A DENSITY INDEPENDENT FORMULATION OF SMOOTHED PARTICLE HYDRODYNAMICS

Takayuki R.Saitoh[1] & Junichiro Makino[1]
Draft version February 26, 2013

ABSTRACT

The standard formulation of the smoothed particle hydrodynamics (SPH) assumes that the local density distribution is differentiable. This assumption is used to derive the spatial derivatives of other quantities. However, this assumption breaks down at the contact discontinuity. At the contact discontinuity, the density of the low-density side is overestimated while that of the high-density side is underestimated. As a result, the pressure of the low (high) density side is over (under) estimated. Thus, unphysical repulsive force appears at the contact discontinuity, resulting in the effective surface tension. This tension suppresses fluid instabilities. In this paper, we present a new formulation of SPH, which does not require the differentiability of density. Instead of the mass density, we adopt the internal energy density (pressure), and its arbitrary function, which are smoothed quantities at the contact discontinuity, as the volume element used for the kernel integration. We call this new formulation density independent SPH (DISPH). It handles the contact discontinuity without numerical problems. The results of standard tests such as the shock tube, Kelvin-Helmholtz and Rayleigh-Taylor instabilities, point like explosion, and blob tests are all very favorable to DISPH. We conclude that DISPH solved most of known difficulties of the standard SPH, without introducing additional numerical diffusion or breaking the exact force symmetry or energy conservation. Our new SPH includes the formulation proposed by Ritchie & Thomas (2001) as a special case. Our formulation can be extended to handle a non-ideal gas easily.

Keywords: galaxies:evolution—galaxies:ISM—methods:numerical

1. INTRODUCTION

Smoothed particle hydrodynamics (SPH) is a Lagrangian scheme to solve the evolution of fluid using particles. It was originally introduced by Lucy (1977) and Gingold & Monaghan (1977) and has been widely used in the field of the computational astrophysics (Monaghan 1992, 2005; Rosswog 2009; Springel 2010b). It is becoming popular in hydrodynamical simulations in engineering (e.g., Liu & Liu 2003).

Recently, Agertz et al. (2007) reported the results of comparison of SPH and Euler schemes (grid methods). Their main finding is that SPH suppresses the Kelvin-Helmholtz instability. This has been pointed out earlier by Okamoto et al. (2003). The reason of this problem is that in the standard SPH the smoothed density is used to obtain other physical quantities. The estimated density of particles near the contact discontinuity has $\mathcal{O}(1)$ error, irrespective of the numerical resolution. This large error causes similarly large error in the pressure (see §2). Agertz et al. (2007) noted that there were *fundamental differences* between SPH and grid methods.

There have been several proposals to improve SPH so that it can deal with the contact discontinuity. Price (2008) discussed the artificial thermal conductivity which was originally introduced by Monaghan (1997). The motivation of the use of the artificial conductivity is that every physical quantity should be *smooth* in the standard SPH. The artificial conductivity eliminates the discontinuity in the thermal energy. Since both the density and energy (entropy) near the contact discontinuity become smooth, the pressure across the contact discontinuity be-

saitoh@geo.titech.ac.jp
[1] Earth-Life Science Institute, Tokyo Institute of Technology, 2–12–1, Ookayama, Meguro, Tokyo, 152-8551, Japan

comes smooth. Thus, the Kelvin-Helmholtz instability takes place. At the first sight, this artificial conductivity looks similar to the artificial viscosity which is necessary to capture shocks in SPH. However, there are two fundamental differences. First, the artificial viscosity is used to generate the physical dissipation associated with the shock, while the artificial conductivity adds physically non-existent dissipation. One needs to fine-tune the conductivity coefficient to prevent unnecessary smoothing. This means that the conductivity must be nonlinear. Second, if there is a jump in the chemical composition, thermal conductivity is not enough. However, whether the use of artificial chemical diffusion is justified or not is an open question. He also showed that, when the Ritchie & Thomas formulation (Ritchie & Thomas 2001) was used, the Kelvin-Helmholtz instability grew but the growth of the instability was insufficient. Read et al. (2010) suggested that the Kelvin-Helmholtz instability took place when a higher order kernel with a large enough number of neighbor particles and the momentum equation of the Ritchie & Thomas (2001) were used. Abel (2011) used the relative pressure, which was first proposed by Morris (1996), instead of the absolute values of pressures in the equation of motion. This formulation improves the treatment of the Kelvin-Helmholtz instability, but breaks the Newton's third law. García-Senz et al. (2012) considered the use of the integral form of the first derivative, which also improved the treatment of hydrodynamical instabilities.

In this paper, we describe a new formulation of SPH which does not use the smoothed mass density for the volume element. Instead, we use an arbitrary function of the internal energy density (pressure) for the volume element to obtain other quantities and their spatial deriva-

tives. The reason why we adopt the energy density instead of the mass density is that it is the fundamental quantity of the hydrodynamics. We call this new formulation density independent SPH (DISPH). In DISPH, the pressure is calculated without using the mass density. Thus, unphysical jumps of pressure at the contact discontinuity disappear. The special case that the volume element defined by the internal energy density or pressure leads to the equation of motion proposed by Ritchie & Thomas (2001). Our formulation can be used to derive the SPH equation for an arbitrary quantity, while how we can apply the Ritchie & Thomas formulation to equations other than energy equation and equation of motion is not clear. Results of various tests indicate that our formulation is highly advantageous.

The structure of this paper is as follows. In §2, we analyze the problem of standard SPH at discontinuities. The derivation of DISPH is described in §3. We then generalized DISPH adopting an arbitrary function of pressure in §4. The comparison of the results of test calculations with DISPH and standard formulation of SPH are shown in §5. Summary and discussion are presented in §6.

2. STANDARD SPH AND ITS DIFFICULTY AROUND DISCONTINUITIES

In SPH, the fluid is expressed by discrete particles and physical quantities are approximated by kernel interpolation. In the standard formulation of SPH, the local density is first calculated, and then the rests of necessary physical quantities, such as the pressure gradient and the time derivative of the internal energy, are calculated. Thus, the accuracy of the solution depends on the accuracy of the density estimate. In this section, we re-examine the derivation of the equation of motion in SPH to understand its problem.

A physical quantity f at position $\boldsymbol{r}$ can be expressed as follows:

$$f(\boldsymbol{r}) = \int f(\boldsymbol{r}')\delta(|\boldsymbol{r} - \boldsymbol{r}'|)d\boldsymbol{r}'. \qquad (1)$$

A smoothed value of f at position $\boldsymbol{r}$, $\langle f \rangle(\boldsymbol{r})$, is given by the convolution of f and a kernel function $W(\boldsymbol{r} - \boldsymbol{r}', h)$:

$$\langle f \rangle(\boldsymbol{r}) = \int f(\boldsymbol{r}')W(|\boldsymbol{r} - \boldsymbol{r}'|, h)d\boldsymbol{r}', \qquad (2)$$

where h is the size of the kernel function and corresponds to the spatial resolution. This smoothing is the base of SPH. Here, the kernel function must satisfy the following three conditions: (1) it becomes the delta function in the limit of $h \to 0$, (2) it is normalized as unity, and (3) it is a function with compact support. A cubic spline function is most widely used as the kernel function:

$$W(|\boldsymbol{r}-\boldsymbol{r}'|, h) = \frac{\sigma}{h^D} \begin{cases} \left(1 - \frac{3}{2}s^2 + \frac{3}{4}s^3\right) & 0 \le s < 1, \\ \frac{1}{4}(2 - s)^3 & 1 \le s < 2, \\ 0 & 2 \le s, \end{cases} \quad (3)$$

where $s = |\boldsymbol{r} - \boldsymbol{r}'|/h$, D is the dimension, and the normalized factors σ in one, two, and three dimensions are $2/3$, $10/7\pi$, and $1/\pi$, respectively. We first derive the equations of motion and energy with the constant kernel size, and then we generalized them to the individual kernel size.

The first derivative of the smoothed f is given by

$$\langle \nabla f \rangle(\boldsymbol{r}) = \int \nabla f(\boldsymbol{r}')W(|\boldsymbol{r} - \boldsymbol{r}'|, h)d\boldsymbol{r}'. \qquad (4)$$

By making use of the partial integral and the fact that the kernel function has compact support, Eq. (4) becomes

$$\langle \nabla f \rangle(\boldsymbol{r}) = \int f(\boldsymbol{r}')\nabla W(|\boldsymbol{r} - \boldsymbol{r}'|, h)d\boldsymbol{r}'. \qquad (5)$$

We need to discretize Eq. (2) to evaluate the physical quantities at positions of particles. To convert integral into summation, a volume element $d\boldsymbol{r}'$ is replaced by the discrete volume element $\Delta V_j = m_j/\rho_j$, where m_j and ρ_j are the mass and density of the particle j. In addition, positions of particles i and j are expressed by $\boldsymbol{r}_i$ and $\boldsymbol{r}_j$ and $f(\boldsymbol{r}')$ is replaced by f_j. Thus, the value of f at the position of particle i is

$$f_i = \sum_j m_j \frac{f_j}{\rho_j} W_{ij}(h), \qquad (6)$$

where $f_i \equiv \langle f \rangle(\boldsymbol{r}_i)$ and $W_{ij} = W(|\boldsymbol{r}_i - \boldsymbol{r}_j|, h)$. Hereafter, we call the SPH formulation with this type of discretization as the *standard SPH*. At this point, we do not know ρ_j. By substituting ρ into f, we obtain

$$\rho_i = \sum_j m_j W_{ij}(h), \qquad (7)$$

where $\rho_i \equiv \langle \rho \rangle(\boldsymbol{r}_i)$ is the smoothed density at the position of particle i. Note that the right-hand side of Eq. (7) includes no unknown quantities. Thus, densities should be calculated first in the standard SPH.

The equation of motion is

$$\frac{d^2\boldsymbol{r}}{dt^2} = -\frac{\nabla P}{\rho}, \qquad (8)$$

where t is time and P is pressure. The SPH approximation of Eq. (8) is given by

$$\frac{d^2\boldsymbol{r}_i}{dt^2} = -\sum_j m_j \left(\frac{P_i}{\rho_i^2} + \frac{P_j}{\rho_j^2}\right)\nabla W_{ij}(h). \qquad (9)$$

This form satisfies the Newton's third law. We used the following relation to obtain Eq. (9):

$$\frac{\nabla P}{\rho} = \nabla\left(\frac{P}{\rho}\right) - \frac{P}{\rho^2}\nabla\rho. \qquad (10)$$

In order for Eq. (9) to be meaningful, ρ must be differentiable, since its derivative is used in Eq. (10).

Finally, we derive the energy equation in the standard SPH. The energy equation is

$$\frac{du}{dt} = -\frac{P}{\rho}\nabla \cdot \boldsymbol{v}, \qquad (11)$$

where u is the internal energy and $\boldsymbol{v}$ is the velocity. To obtain the SPH formulation of the energy equation, we need the SPH expression of $\nabla \cdot \boldsymbol{v}$. We use

$$\nabla(\rho\boldsymbol{v}) = \nabla\rho\boldsymbol{v} + \rho\nabla \cdot \boldsymbol{v}. \qquad (12)$$

The SPH formulation of $\nabla \cdot \boldsymbol{v}$ is given by

$$\rho_i \nabla \cdot \boldsymbol{v}_i = \sum_j m_j \boldsymbol{v}_j \cdot \nabla W_{ij}(h) - \boldsymbol{v}_i \cdot \sum_j m_j \nabla W_{ij}(h)$$

$$= -\sum_j m_j \boldsymbol{v}_{ij} \cdot \nabla W_{ij}(h), \qquad (13)$$

where $\boldsymbol{v}_{ij} = \boldsymbol{v}_i - \boldsymbol{v}_j$. Therefore, the energy equation in the standard SPH is

$$\frac{du_i}{dt} = \sum m_j \frac{P_i}{\rho_i^2} \boldsymbol{v}_{ij} \cdot \nabla W_{ij}(h). \qquad (14)$$

Equations (7), (9), and (14) close with the equation of state (EOS),

$$P = (\gamma - 1)\rho u, \qquad (15)$$

where γ is the specific heat ratio. There is no need to solve the continuity equation in SPH since it is satisfied automatically.

When we use the variable and individual kernel size, above equations should be modified slightly. Here, we adopt a simple and traditional way. First, the density evaluation equation is rewritten as

$$\rho_i = \sum_j m_j W_{ij}(h_i). \qquad (16)$$

This is the same as so-called gather interpretation of the summation (Hernquist & Katz 1989). When a variable kernel size is employed, an iterative approach is used to determine both ρ and h imposing a condition, for instance, that the number of neighbor particles is kept in a fixed range. In equations of motion and energy, the gather-and-scatter interpretation is used (Hernquist & Katz 1989). Thus, Eqs. (9) and (14) become

$$\frac{d^2 \boldsymbol{r}_i}{dt^2} = -\sum_j m_j \left(\frac{P_i}{\rho_i^2} + \frac{P_j}{\rho_j^2} \right) \nabla \tilde{W}_{ij}, \qquad (17)$$

and

$$\frac{du_i}{dt} = \sum_j m_j \frac{P_i}{\rho_i^2} \boldsymbol{v}_{ij} \cdot \nabla \tilde{W}_{ij}, \qquad (18)$$

where $\nabla W_{ij}(h_i)$ is replaced by $\nabla \tilde{W}_{ij} = 0.5[\nabla W_{ij}(h_i) + \nabla W_{ij}(h_j)]$ so that the equation of motion can satisfy the Newton's third law. It is also possible to use $\nabla \tilde{W}_{ij} = \nabla W_{ij}[0.5(h_i + h_j)]$. We adopt the first form throughout this paper.

The Lagrangian formulation (Springel & Hernquist 2002) provides the derivative of the kernel size. We will show the comparison results in §5.6.

In the derivation of the standard SPH discretization, the differentiability of ρ is used for both the equation of motion and the energy equation. However, ρ is discontinuous at the contact discontinuity. In the following, we illustrate the consequence of the discontinuity of the density.

In Figure 1, we show the values of density and pressure around a contact discontinuity evaluated by the standard formulation of SPH. Equation (16) is used and $P = (\gamma - 1)\rho u$. To set up this contact discontinuity, we place particles on a regular grid in three dimensions and set $\rho = 1$ for $x < 0.5$ and $\rho = 0.125$ for $x > 0.5$. We used

equal-mass particles in the first two configurations. In these two setups, positions of particles in the less dense region is determined by taking the center of mass of the eight particles in the cube of the particle separation. In the last configuration, we adopted the equal separation for both regions, which means that the mass of particles in the less dense region is 1/8 of that of particles in the dense region. The internal energy was set to 1.5 ($x < 0.5$) and 12 ($x > 0.5$), and the specific heat ratio was 5/3. Velocities of particles were set to zero. The kernel size is determined to keep the neighbor number, $N_{\rm nb}$, to the range 32 ± 2, in the first and the last tests. In the second test a constant h fixed to twice the particle separation in the less dense region is used.

The top panels show the distribution of particles. The panels in the second row show the SPH density. Though the initial setup has the discontinuity at $x = 0.5$, it is smoothed by the kernel. As a result, the SPH density of particles next to the discontinuity has very large errors, as shown in the panels in the 3rd row. This large error in the density causes similarly large error in the pressure (4th row). The pressure of particles at the end of the low-density region is grossly overestimated, while that at the end of the high-density region is underestimated only modestly. This non-symmetric error in the pressure is the origin of the repulsive force at the contact discontinuity, as has been pointed out in previous studies (e.g., Ritchie & Thomas 2001; Okamoto et al. 2003; Agertz et al. 2007). This large error in the pressure also exists in both of the constant kernel size case (the middle column) and the equal-separation case (the right column).

Consider the following density and pressure distribution:

$$\rho = \begin{cases} \rho_1 & x \geq 0, \\ \rho_2 & x < 0, \end{cases} \qquad (19)$$

and

$$P = P_0. \qquad (20)$$

Obviously, we have

$$\langle \rho \rangle (x) \to \frac{\rho_1 + \rho_2}{2}, \quad \text{for } x \to 0, \qquad (21)$$

and therefore,

$$\lim_{x \to +0} \langle P \rangle (x) = \frac{\rho_1 + \rho_2}{2\rho_1} P_0, \qquad (22)$$

$$\lim_{x \to -0} \langle P \rangle (x) = \frac{\rho_1 + \rho_2}{2\rho_2} P_0. \qquad (23)$$

Thus, if $\rho_1 \ll \rho_2$, the error of the pressure can be arbitrarily large. Note that the existence of this error does not imply the inconsistency of SPH. In this limit of $h \to 0$, the volume of the regime affected by this error approaches to zero, which means the original differential equation is restored almost everywhere. In other words, SPH satisfies the weak form of the original equation. However, it means the convergence is slow and first order.

One might think that this error is caused by an inadequate initial thermal energy (or density) distribution. However, it is not the case. If we initialize the internal energy (and/or density) of particles near the contact discontinuity so that the pressure is smooth initially, this is no problem. However, as the particles
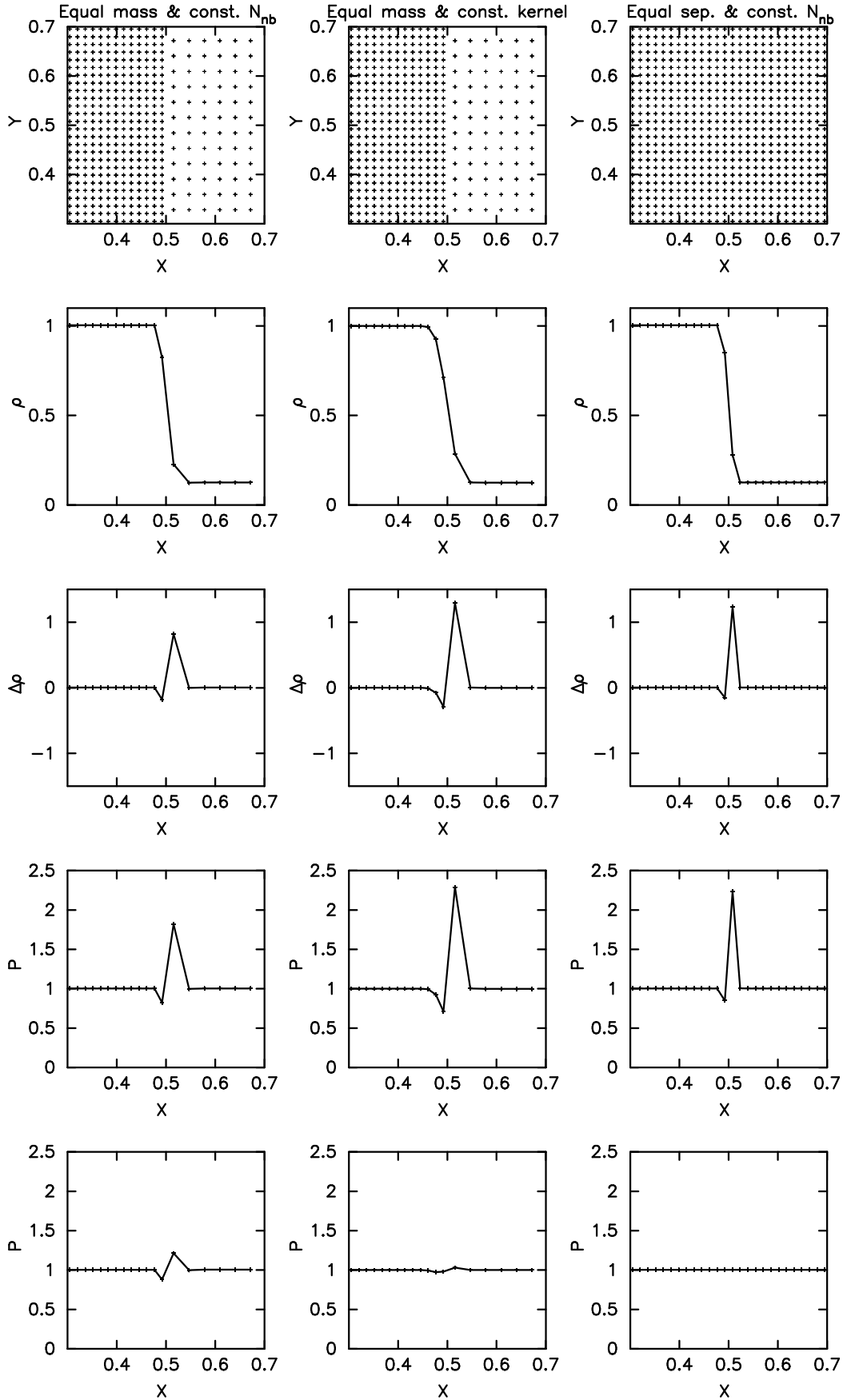
Figure 1. Density and pressure fields evaluated with the standard SPH and our SPH around the contact discontinuity with the density ratio of 1 : 8. Equal mass particles are used for the first and second configurations (the left and middle columns). The positions of the less dense region is determined by taking the center of mass of the eight particles in the cube of the particle separation. The equal separation is used in the last configuration (the right column). In this configuration, the mass of particles in the less dense region is 1/8 of that of particles in the dense region. For the left and right columns, the constant neighbor number, 32 ± 2, is used. In the middle column, a constant kernel size of 0.03125 is used. The top row shows the distribution of particles projected on the $x - y$ plane. The second row shows the density of each SPH particle evaluated with Eq. (16). The third row shows the density contrast between the evaluated density and true one. The fourth row shows corresponding pressure. In the bottom row, the pressure of each particle calculated with DISPH is shown.

move, the change of the density can become sharpen, resulting in the numerical problem described above. We, thus, need continuous adjustment to suppress the pressure error throughout the time integration. Price's artificial conductivity (Price 2008) provides such a continuous adjustment. Though the artificial conductivity works beautifully in test calculations for the Kelvin-Helmholtz instability, whether its use in actual astrophysical simulation is justified or not is a bit questionable. First, in the case of the discontinuity of chemical composition, not only the jump in the internal energy but also that in the chemical composition should be smoothed but that is clearly not adequate. Second, the artificial heat conduction can significantly enhance the thermal relaxation of the system, which is again unwanted.

3. A DENSITY INDEPENDENT FORMULATION OF SPH

In §2, we have seen that the standard SPH breaks down at the contact discontinuity because the continuity and differentiability of the density is necessary to guarantee the convergence of SPH approximation. The basic reason for this problem is the use of m_j/ρ_j for the volume element. Thus, if we use something else as the volume element, we might be able to avoid this difficulty altogether. As shown in §4, the formulation we show in this section is the special case of the density independent formulation of SPH.

3.1. Concept

Here, we propose an alternative formulation of SPH in which we discretize Eq. (2) using the EOS of fluid, not the mass density. The new volume element of j-th particle is

$$d\boldsymbol{r}' = \Delta V_j = \frac{(\gamma - 1)m_j u_j}{P_j} = \frac{U_j}{q_j}, \qquad (24)$$

where $q_j \equiv \rho_j u_j$ and $U_j = m_j u_j$ are the energy density and the internal energy of particle j, respectively. Substituting Eq. (24) into Eq. (2) and using the gather summation, we obtain a new SPH approximation of smoothed f:

$$f_i = \sum_j (\gamma - 1)\frac{m_j u_j f_j}{P_j} W_{ij}(h_i), \qquad (25)$$

$$= \sum_j (\gamma - 1)\frac{U_j f_j}{P_j} W_{ij}(h_i). \qquad (26)$$

By substituting f with the energy density, q, we have

$$q_i = \sum_j U_j W_{ij}(h_i). \qquad (27)$$

where we used $q_i \equiv \langle q \rangle(\boldsymbol{r})$. By replacing $d\boldsymbol{r}'_j$ in Eq. (5) with Eq. (24), we have the gradient of $\langle f \rangle$:

$$\langle \nabla f \rangle(\boldsymbol{r}_i) = \sum_j U_j \frac{f_j}{q_j} \nabla W_{ij}(h_i). \qquad (28)$$

We adopt Eqs. (26) and (27) as the basis of DISPH. We derive the equations of motion and energy from this basis. We note that DISPH is also Galilei invariant.

One might think that the use of U for the calculation of the volume element would cause some inconsistency,

since U is not a conserved quantity. The mass of a particle is constant, and thus looks safer. In the following, we show that we can construct a consistent set of equations using U, and that it has many advantages over the standard SPH and that it retains important characteristics such as force symmetry and energy conservation. We first derive the energy equation and then equation of motion. We then discuss the formulation for the estimate of the density and the implementation of the artificial viscosity.

3.2. Energy Equation

We need an expression of $\nabla \cdot \boldsymbol{v}$ to derive the energy equation. We start with

$$\nabla(q\boldsymbol{v}) = \nabla q\boldsymbol{v} + q\nabla \cdot \boldsymbol{v}, \qquad (29)$$

which is obtained by replacing ρ in Eq. (12) with q. By applying Eq. (28) to Eq. (29), we obtain an analogy of Eq. (13):

$$q_i \nabla \cdot \boldsymbol{v}_i = \sum_j U_j \boldsymbol{v}_j \cdot \nabla W_{ij}(h_i) - \boldsymbol{v}_i \cdot \sum_j U_j \nabla W_{ij}(h_i)$$

$$= -\sum_j U_j \boldsymbol{v}_{ij} \cdot \nabla W_{ij}(h_i). \qquad (30)$$

The energy equation is then given by

$$\frac{du_i}{dt} = \sum_j U_j \frac{P_i}{\rho_i q_i} \boldsymbol{v}_{ij} \cdot \nabla \tilde{W}_{ij}. \qquad (31)$$

Equation (31) contains ρ_i since u is the energy per unit mass. The equation for U_i is obtained by multiplying Eq. (31) by m_i:

$$\frac{dU_i}{dt} = \frac{m_i}{\rho_i} \sum_j \frac{U_j P_i}{q_i} \boldsymbol{v}_{ij} \cdot \nabla \tilde{W}_{ij}. \qquad (32)$$

Here, m_i/ρ_i is the volume associated with particle i which can be replaced by $U_i/q_i = (\gamma - 1)U_i/P_i$. Thus, we have

$$\frac{dU_i}{dt} = (\gamma - 1) \sum_j \frac{U_i U_j}{q_i} \boldsymbol{v}_{ij} \cdot \nabla \tilde{W}_{ij}. \qquad (33)$$

3.3. Equation of Motion

From the energy equation, Eq. (33), we derive the equation of motion. The change in the internal energy of particles i and j due to their relative motion is

$$\frac{dU_i}{dt} + \frac{dU_j}{dt} = (\gamma - 1)U_i U_j \left(\frac{1}{q_i} + \frac{1}{q_j}\right) \boldsymbol{v}_{ij} \cdot \nabla \tilde{W}_{ij}. \quad (34)$$

This change is the same as the change of the kinetic energy of particles with an opposite sign. Thus, we have

$$\frac{m_i m_j}{m_i + m_j} \boldsymbol{v}_{ij} \cdot \left(\frac{d\boldsymbol{v}_i}{dt} - \frac{d\boldsymbol{v}_j}{dt}\right) = -\left(\frac{dU_i}{dt} + \frac{dU_j}{dt}\right). \quad (35)$$

Substituting Eq. (34) into Eq. (35), we obtain

$$\left(\frac{d\boldsymbol{v}_i}{dt} - \frac{d\boldsymbol{v}_j}{dt}\right) = -(\gamma - 1)\frac{m_i + m_j}{m_i m_j} U_i U_j \left(\frac{1}{q_i} + \frac{1}{q_j}\right) \nabla \tilde{W}_{ij}. \tag{36}$$

Since the motion of the center of mass of two particles is unchanged by the interaction of two particle, we have

$$\frac{d}{dt}(m_i \boldsymbol{v}_i + m_j \boldsymbol{v}_j) = 0. \quad (37)$$

Thus, we have

$$m_i \frac{d\boldsymbol{v}_i}{dt} = -(\gamma - 1)U_i U_j \left(\frac{1}{q_i} + \frac{1}{q_j}\right) \nabla \tilde{W}_{ij}, \quad (38)$$

as the contribution of particle j to the equation of motion of particle i.

The equation of motion for particle i is obtained by taking summation over neighbor particles:

$$m_i \frac{d\boldsymbol{v}_i}{dt} = -(\gamma - 1) \sum_j U_i U_j \left(\frac{1}{q_i} + \frac{1}{q_j}\right) \nabla \tilde{W}_{ij}. \quad (39)$$

The right-hand side of Eq. (39) contains only the energy U and energy density q. Thus, as far as q is smooth, Eq. (39) is likely to be well-behaved. The equation of motion of the standard SPH [Eq. (9)] requires that both P and ρ are smooth. Thus, in our formulation, there is nothing special about the contact discontinuity. We can therefore expect that the treatment of the contact discontinuity is improved. We will see this in §3.6.

Note that Eq. (39) is mathematically equivalent to the equation of motion obtained by Ritchie & Thomas (2001), while the derivation is completely different. Ritchie & Thomas (2001) started from Eq. (27) and density estimate $\rho = mq/U$, but still tried to use standard SPH estimate of Eq. (6). In order to eliminate ρ from equation of motion, they used the following formal relationship

$$\frac{\nabla P}{\rho} = \frac{\nabla P}{\rho} + \frac{P}{\rho} \nabla 1, \quad (40)$$

and formal identity

$$\nabla 1 = \sum_j m_j \frac{1}{\rho_j} \nabla W_{ij}(h) \simeq 0. \quad (41)$$

Thus, their derivation was a heuristic modification of the standard SPH and they did not employ the volume element $(\gamma - 1)m_j u_j / P_j$ explicitly. We have shown that by choosing $(\gamma - 1)m_j u_j / P_j$ as the volume element, we can derive a consistent set of SPH equations naturally.

3.4. Artificial Viscosity

To deal with shocks, the standard SPH needs an artificial viscosity term. DISPH also needs an artificial viscosity term. We utilize artificial viscosity terms which are widely used in simulations with the standard SPH.

The viscosity term for the equation of motion is

$$m_i \frac{d^2 \boldsymbol{r}_i}{dt^2} = -m_i \sum_j m_j \Pi_{ij} \nabla \tilde{W}_{ij}, \quad (42)$$

and the corresponding form of it for the energy equation is

$$\frac{dU_i}{dt} = \frac{m_i}{2} \sum_j m_j \Pi_{ij} \boldsymbol{v}_{ij} \cdot \nabla \tilde{W}_{ij}, \quad (43)$$

where Π_{ij} is the function of the strength of the artificial viscosity.

There are two types of artificial viscosity term, Π_{ij}, which are commonly used. The most commonly used one (Lattanzio et al. 1985) is

$$\Pi_{ij} = \begin{cases} \frac{-\alpha c_{ij} \mu_{ij} + \beta \mu_{ij}^2}{\rho_{ij}} & \boldsymbol{v}_{ij} \cdot \boldsymbol{r}_{ij} < 0, \\ 0 & \boldsymbol{v}_{ij} \cdot \boldsymbol{r}_{ij} \geq 0, \end{cases} \quad (44)$$

where α and β are the control parameters for the strength of the artificial viscosity, c_{ij} is the arithmetic average of the sound speeds of particles i and j, $\rho_{ij} = 0.5(\rho_i + \rho_j)$, and

$$\mu_{ij} = \frac{h_{ij} \boldsymbol{v}_{ij} \cdot \boldsymbol{r}_{ij}}{r_{ij}^2 + \epsilon h_{ij}^2}. \quad (45)$$

The constant ϵ is introduced to avoid the divergence and its fiducial value is ~ 0.01.

The other one is proposed by Monaghan (1997) from the analogy of the Riemann solver:

$$\Pi_{ij} = \begin{cases} -\frac{\alpha}{2} \frac{v_{ij}^{\mathrm{sig}} w_{ij}}{\rho_{ij}} & \boldsymbol{v}_{ij} \cdot \boldsymbol{r}_{ij} < 0, \\ 0 & \boldsymbol{v}_{ij} \cdot \boldsymbol{r}_{ij} \geq 0, \end{cases} \quad (46)$$

where $v_{ij}^{\mathrm{sig}} = c_i + c_j - 3w_{ij}$ and $w_{ij} = \boldsymbol{v}_{ij} \cdot \boldsymbol{r}_{ij} / r_{ij}$.

Since we have the density estimate $\rho = q/u$, we have

$$\rho_{ij} = \frac{1}{2} \left(\frac{q_i}{u_i} + \frac{q_j}{u_j}\right), \quad (47)$$

for our formulation. However, this modification of ρ_{ij} leads to unstable behavior under strong shocks. It seems to be safe to use the smoothed mass densities of particles i and j evaluated using Eq. (7). The viscosity relates to the inertial force. Therefore, the use of the matter distribution is reasonable. We use the smoothed mass density to evaluate the artificial viscosity term. In §5.6, we investigate the effect of the choice of the averaged density in the artificial viscosity term. It is also safer to use the smoothed mass density, when one use our SPH for the simulation with a radiative cooling term.

We use the standard Balsara switch (Balsara 1995) to suppress the shear viscosity. It is given by

$$F_i^{\mathrm{Balsara}} = \frac{|\nabla \cdot \boldsymbol{v}_i|}{|\nabla \cdot \boldsymbol{v}_i| + |\nabla \times \boldsymbol{v}_i| + \epsilon_b c_i / h_i}, \quad (48)$$

and $\Pi_{ij}^{\mathrm{Balsara}} = 0.5(F_i^{\mathrm{Balsara}} + F_j^{\mathrm{Balsara}})\Pi_{ij}$. Here ϵ_b is a small value (typically 10^{-4}). The rotation of velocity in the standard SPH is found in literature (e.g., Monaghan 1992). The rotation of velocity in our SPH is calculated as follows:

$$\nabla \times \boldsymbol{v}_i = \frac{1}{q_i} \sum_j U_j \boldsymbol{v}_{ij} \times \nabla W_{ij}(h_i). \quad (49)$$

3.5. Grad-h Term

To obtain a consistent formulation with the variable kernel size, we have to take into account not only the gradient of kernel and physical quantities respect to r but also that respect to h. Here, we take the contribution of the variable kernel size into account. This was accomplished by using the Lagrangian formulation (Springel & Hernquist 2002; Rosswog 2009; Springel 2010a; Hopkins 2013). Since the variation of h is the first order term, the contribution of this term is rather limited. Indeed,

we find that the contribution of this term is prominent only in extremely strong shock problems like the Sedov problem (See §5.6).

We start from the Lagrangian:

$$L(\dot{\boldsymbol{Q}}, \boldsymbol{Q}) = \sum_i \frac{1}{2} m_i \dot{\boldsymbol{Q}}_i^2 - \sum_i U_i(\boldsymbol{Q}), \qquad (50)$$

where $\boldsymbol{Q} \equiv (\boldsymbol{r}_1, \boldsymbol{r}_2, , , \boldsymbol{r}_N, h_1, h_2, , , h_N)$. We adopt the following constraint:

$$\phi_i = \frac{4\pi}{3} (2h_i)^3 \frac{q_i}{U_i} - N_{\mathrm{ngb}} = 0. \qquad (51)$$

This constraint means that the spherical region with the radius $2h_i$ covers a volume of $N_{\mathrm{ngb}} \Delta V_i$.

The Euler-Lagrange equation with a constraint is as follows:

$$\frac{d}{dt} \frac{\partial L}{\partial \dot{\boldsymbol{Q}_i}} - \frac{\partial L}{\partial \boldsymbol{Q}_i} = \sum_j \lambda_j \frac{\partial \phi_j}{\partial \boldsymbol{Q}_i}. \qquad (52)$$

First, we solve this equation regarding the kernel size. Since the Lagrangian and constraint do not have the first order derivative of the kernel size, Eq. (52) is

$$-\frac{\partial L}{\partial h_i} = \sum_j \lambda_j \frac{\partial \phi_j}{\partial h_i}. \qquad (53)$$

The left-hand-side of this equation is

$$\begin{aligned}
-\frac{\partial L}{\partial h_i} &= \frac{\partial U_i}{\partial h_i}, \\
&= \frac{\partial U_i}{\partial \Delta V_i} \frac{\partial \Delta V_i}{\partial q_i} \frac{\partial q_i}{\partial h_i}, \\
&= \frac{P_i U_i}{q_i^2} \frac{\partial q_i}{\partial h_i}, \qquad (54)
\end{aligned}$$

where we used the first law of thermodynamic in an adiabatic state, $dU = -PdV$.

The right-hand-side of Eq. (53) is

$$\begin{aligned}
\sum_j \lambda_j \frac{\partial \phi_j}{\partial h_i} &= \sum_j \lambda_j \frac{\partial}{\partial h_i} \left[\frac{4\pi}{3} (2h_j)^3 \frac{q_j}{U_j} - N_{\mathrm{ngb}} \right], \\
&= \lambda_i 32\pi h_i^2 \frac{q_i}{U_i} \left(1 + \frac{h_i}{3q_i} \frac{\partial q_i}{\partial h_i} \right). \qquad (55)
\end{aligned}$$

Hence, we have

$$\lambda_i = \frac{3P_i}{32\pi h_i^3} \frac{U_i^2}{q_i^2} \psi_i, \qquad (56)$$

where

$$\psi_i = \frac{h_i}{3q_i} \frac{\partial q_i}{\partial h_i} \left(1 + \frac{h_i}{3q_i} \frac{\partial q_i}{\partial h_i} \right)^{-1}. \qquad (57)$$

Next, let's solve the Euler-Lagrange equation regarding $\boldsymbol{r}$. According to Eq. (52), the equation of motion is

$$\begin{aligned}
m_i \frac{dv_i}{dt} &= -\nabla_i \sum_j U_j + \sum_j \lambda_j \nabla_i \phi_j \\
&= -\sum_j \frac{\partial U_j}{\partial \Delta V_j} \nabla_i \Delta V_j
\end{aligned}$$

$$\begin{aligned}
&+ \sum_j \frac{3P_j}{32\pi h_j^3} \frac{U_j^2}{q_j^2} \psi_j \nabla_i \left[\frac{4\pi}{3} (2h_j)^3 \frac{q_j}{U_j} - N_{\mathrm{ngb}} \right] \\
&= -\sum_j \frac{P_j U_j}{q_j^2} (1 - \psi_j) \nabla_i q_j \\
&= -\sum_j \frac{P_j U_j}{q_j^2} f_j^{\mathrm{grad}} \nabla_i q_j, \qquad (58)
\end{aligned}$$

where

$$f_j^{\mathrm{grad}} \equiv (1 - \psi_j) = \left(1 + \frac{h_j}{3q_j} \frac{\partial q_j}{\partial h_j} \right)^{-1}. \qquad (59)$$

By using

$$\begin{aligned}
\nabla_i q_j &= \nabla_i \sum_k U_k W_{jk}(h_j) \\
&= U_i \nabla_i W_{ij}(h_j) + \delta_{ij} \sum_k U_k \nabla_i W_{ik}(h_i), \\
& \qquad\qquad\qquad\qquad\qquad\qquad\qquad (60)
\end{aligned}$$

equation (58) becomes

$$\begin{aligned}
m_i \frac{dv_i}{dt} &= -\sum_j \frac{P_j U_j}{q_j^2} f_j^{\mathrm{grad}} \\
&\qquad \left(U_i \nabla_i W_{ij}(h_j) + \delta_{ij} \sum_k U_k \nabla_i W_{ik}(h_i) \right), \\
&= -(\gamma - 1) \sum_j U_i U_j \\
&\qquad \left(\frac{1}{q_i} f_i^{\mathrm{grad}} \nabla_i W_{ij}(h_i) + \frac{1}{q_j} f_j^{\mathrm{grad}} \nabla_i W_{ij}(h_j) \right). \\
& \qquad\qquad\qquad\qquad\qquad\qquad\qquad (61)
\end{aligned}$$

The energy equation can be obtained as follows:

$$\begin{aligned}
\frac{dU_i}{dt} &= -P_i \frac{d\Delta V_i}{dt}, \\
&= P_i \frac{U_i}{q_i^2} \frac{dq_i}{dt}. \qquad (62)
\end{aligned}$$

Taking a time derivative of q_i, we have

$$\begin{aligned}
\frac{dq_i}{dt} &= \frac{d}{dt} \sum_j U_j W_{ij}(h_i), \\
&= \sum_j U_j \frac{d\boldsymbol{r}_{ij}}{dt} \cdot \nabla_i W_{ij}(h_i) + \sum_j U_j \frac{dh_i}{dt} \frac{\partial W_{ij}(h_i)}{\partial h_i}, \\
&= \sum_j U_j \boldsymbol{v}_{ij} \cdot \nabla_i W_{ij}(h_i) + \frac{dq_i}{dt} \frac{\partial h_i}{\partial q_i} \sum_j U_j \frac{\partial W_{ij}(h_i)}{\partial h_i}. \\
& \qquad\qquad\qquad\qquad\qquad\qquad\qquad (63)
\end{aligned}$$

Then,

$$\left(1 - \frac{\partial h_i}{\partial q_i} \sum_j U_j \frac{\partial W_{ij}(h_i)}{\partial h_i} \right) \frac{dq_i}{dt} = \sum_j U_j \boldsymbol{v}_{ij} \cdot \nabla_i W_{ij}(h_i). \qquad (64)$$

Since $h_i^3 q_i = \text{const}$, we have

$$\left(\frac{\partial h_i}{\partial q_i}\right)^{-1} = -3\frac{q_i}{h_i}. \qquad (65)$$

Therefore, Eq (64) becomes

$$\left(1 + \frac{h_i}{3q_i}\frac{\partial q_i}{\partial h_i}\right)\frac{dq_i}{dt} = \sum_j U_j \boldsymbol{v}_{ij} \cdot \nabla_i W_{ij}(h_i), \qquad (66)$$

and using Eq. (59),

$$\frac{dq_i}{dt} = f_i^{\text{grad}} \sum_j U_j \boldsymbol{v}_{ij} \cdot \nabla_i W_{ij}(h_i). \qquad (67)$$

By substituting Eq. (67) into Eq. (62), we finally obtain the energy equation,

$$\frac{dU_i}{dt} = (\gamma - 1) \sum_j \frac{U_i U_j}{q_i} f_i^{\text{grad}} \boldsymbol{v}_{ij} \cdot \nabla_i W_{ij}(h_i) \qquad (68)$$

This energy equation and the equation of motion, Eq. (61), are also density independent.

The Lagrangian formulation guarantees the conservation of the energy and momentum. We note that the set of equations of energy and motion, Eqs. (33) and (39), also conserve the energy and momentum, since these equations are derived by assuming the conservation of the energy and momentum.

3.6. Pressure in Contact Discontinuities

The pressure around the contact discontinuity calculated with our SPH equation, Eq. (27) is shown in the bottom panels of figure 1. In the case of the equal-mass particle and the fixed neighbor number (the left panel), we can see that the jump of the pressure at the contact discontinuity in DISPH is much smaller than that in the standard SPH. In the case of the constant kernel size (the middle panel), the result of DISPH is almost flat, while that of the standard SPH has a large error.

In these two equal-mass cases, pressure still has small jumps at the contact discontinuity. The reason is that in both cases the distribution of particles is asymmetric. In the high-density region, the particle separation is smaller, resulting in small integration error. As a result, small error appears when the kernel contains the contribution from both low- and high-density regions. In the case of the equal separation of particles, there is no jump in the pressure distribution at the contact discontinuity, as shown in the rightmost panel.

4. A GENERALIZED FORM OF DISPH

In §3, we have derived equations of energy and motion which do not depend on the density in the right-hand-side of them. To derive these formulation, we used q instead of ρ as a basis of the formulation. In an ideal fluid, q is identical to P except the factor of $\gamma - 1$ and the pressure is the continuous quantity across contact discontinuities.

As we will show in the next section, this formulation works quite well in many tests, such as shock tube test, Kelvin-Helmholtz and Rayleigh-Taylor instability tests. However, this formulation is not good for the extremely strong shock tests where the pressure jump at the shock is very large.

In this section, we generalize DISPH by using an arbitrary function of pressure, instead of $q = P/(\gamma - 1)$. If we choose the form of the function that depends weakly on the pressure, such formulation might work well even for the extremely strong shock. As we show in §5.6, we found that it indeed works well. In the following, we derive a generalized form of DISPH.

4.1. Equations of a Generalized DISPH

We start from the following relation:

$$y_i = G(P_i), \qquad (69)$$

where $G(\boldsymbol{P}_i)$ is an arbitrary function of P_i. Formally, any kind of function is possible as G. When we introduce a physical quantity, Z, we can define a new volume element as

$$\Delta V_i = \frac{Z_i}{y_i}. \qquad (70)$$

By applying Eq. (70) to Eq. (2), we have

$$f_i = \sum_j Z_j \frac{f_j}{y_j} W_{ij}(h_i). \qquad (71)$$

When we assume $f = y$, we have

$$y_i = \sum_j Z_j W_{ij}(h_i). \qquad (72)$$

The quantity y given by Eq. (72) is the basic quantity of this generalized DISPH. This is an implicit equation for y and Z. We will show how to solve this equation in §4.3. Here, we continue the deviation of equations. The first derivative of the physical quantity f is given by

$$\langle \nabla f \rangle(\boldsymbol{r}) = \sum Z_j \frac{f_j}{y_j} \nabla W_{ij}(h_i). \qquad (73)$$

The equations of energy and motion are

$$\frac{dU_i}{dt} = \sum_j \frac{P_i Z_i Z_j}{y_i^2} \boldsymbol{v}_{ij} \cdot \nabla \tilde{W}_{ij}, \qquad (74)$$

$$m_i \frac{d\boldsymbol{v}_i}{dt} = -\sum_j Z_i Z_j \left(\frac{P_i}{y_i^2} + \frac{P_j}{y_j^2}\right) \nabla \tilde{W}_{ij}, \qquad (75)$$

where we use the following relation:

$$\nabla(y\boldsymbol{v}) = \nabla y \boldsymbol{v} + y \nabla \cdot \boldsymbol{v}, \qquad (76)$$

which can be rewritten as

$$\nabla \cdot \boldsymbol{v}_i = -\frac{1}{y_i} \sum_j Z_j \boldsymbol{v}_{ij} \cdot \nabla W_{ij}(h_i). \qquad (77)$$

The rotation of velocity in this generalized DISPH is expressed as

$$\nabla \times \boldsymbol{v}_i = \frac{1}{y_i} \sum_j Z_j \boldsymbol{v}_{ij} \times \nabla W_{ij}(h_i). \qquad (78)$$

The time derivative of Z is obtained from Eq. (70). By taking the time derivative of Eq. (70), we have

$$\frac{dZ_i}{dt} = Z_i \left(\frac{1}{\Delta V_i}\frac{\partial \Delta V_i}{\partial t} + \frac{1}{y_i}\frac{\partial y_i}{\partial t}\right),$$

$$= Z_i \left(\frac{1}{\Delta V_i} \frac{\partial \Delta V_i}{\partial t} + \frac{1}{y_i} \frac{\partial \Delta V_i}{\partial t} \frac{\partial y_i}{\partial \Delta V_i} \right),$$

$$= \frac{Z_i}{\Delta V_i} \frac{\partial \Delta V_i}{\partial t} \left(1 + \frac{\Delta V_i}{y_i} \frac{\partial y_i}{\partial \Delta V_i} \right). \qquad (79)$$

Adopting the following relations:

$$\frac{1}{\Delta V_i} \frac{\partial \Delta V_i}{\partial t} = \nabla \cdot \boldsymbol{v}_i, \qquad (80)$$

$$\frac{d \log P_i}{d \log \Delta V_i} = -\gamma, \qquad (81)$$

$$\frac{d \log y_i}{d \log P_i} = \frac{d \log G(P_i)}{d \log P_i} \equiv \zeta(P_i), \qquad (82)$$

we finally obtain

$$\frac{dZ_i}{dt} = Z_i(\zeta(P_i)\gamma - 1)\frac{1}{\Delta V_i}\frac{\partial \Delta V_i}{\partial t},$$

$$= (\zeta(P_i)\gamma - 1)\sum \frac{Z_i Z_j}{y_i}\boldsymbol{v}_{ij} \cdot \nabla W_{ij}(h_i). \qquad (83)$$

Note that these equations is reduced to those of DISPH shown in §3, if we choose q_i as y_i. Thus, the equations of DISPH obtained in §3 is a special case of the generalized DISPH. In this special case, the time derivative of Z is identical to the energy equation.

4.2. A Generalized DISPH with the Grad-h Term

We can obtain the grad-h term by using the new volume element Eq. (70). We begin the derivation by the Lagrangian, Eq. (50), and a constraint with the new volume element of the generalized DISPH,

$$\phi_i = \frac{4\pi}{3}(2h_i)^3 \frac{y_i}{Z_i} - N_{\mathrm{ngb}} = 0. \qquad (84)$$

By solving the Euler-Lagrange equation, we finally obtain the following set of equations:

$$m_i \frac{d\boldsymbol{v}_i}{dt} = -\sum_j Z_i Z_j$$

$$\left(\frac{P_i}{y_i^2} f_i^{\mathrm{grad}} \nabla_i W_{ij}(h_i) + \frac{P_j}{y_j^2} f_j^{\mathrm{grad}} \nabla_i W_{ij}(h_j) \right), \qquad (85)$$

$$\frac{dU_i}{dt} = \frac{P_i Z_i}{y_i^2} f_i^{\mathrm{grad}} \sum_j Z_j \boldsymbol{v}_{ij} \cdot \nabla_i W_{ij}(h_i), \qquad (86)$$

where

$$f_i^{\mathrm{grad}} = \left(1 + \frac{h_i}{3 y_i} \frac{\partial y_i}{\partial h_i} \right)^{-1}. \qquad (87)$$

The time derivative of Z is as follows:

$$\frac{dZ_i}{dt} = (\zeta(P_i)\gamma - 1) f_i^{\mathrm{grad}} \sum \frac{Z_i Z_j}{y_i}\boldsymbol{v}_{ij} \cdot \nabla W_{ij}(h_i). \qquad (88)$$

Again, these equations are reduced to those obtained in §3.5, if we adopt q_i as y_i.

4.3. Solving the Implicit Relation Between y and Z

We have the energy equation [Eq. (74)] and the equation (83) for Z. If we integrate both U and Z, they will

become inconsistent due to the truncation error of the integration scheme. Thus, we should "correct" the value of Z so that it is consistent to U. To solve this matter, we use an iteration method to obtain the consistent value of Z with the equation of state. The procedure is as follows:

1. Predict Z at the next step, $Z_i^{\mathrm{new,p}}$, by calculating

$$Z_i^{\mathrm{new,p}} = Z_i^{\mathrm{old}} + \frac{dZ_i}{dt}dt, \qquad (89)$$

where Z_i^{old} is the value of Z at the last step.

2. Using this $Z_i^{\mathrm{new,p}}$, we obtain y_i^{new} by evaluating Eq. (69).

3. Then, we evaluate the value of Z using y:

$$\hat{Z}_i^{\mathrm{new}} = (y_i^{\mathrm{new}})^{1 - \frac{1}{\zeta(P_i)}}(\gamma - 1)U_i. \qquad (90)$$

4. We update the value of Z:

$$Z_i^{\mathrm{new}} = Z_i^{\mathrm{old}} + \zeta(P_i)(\hat{Z}_i^{\mathrm{new}} - Z_i^{\mathrm{old}}). \qquad (91)$$

5. We again calculate y using Eq. (69):

$$y_i^{\mathrm{new}} = \sum Z_i^{\mathrm{new}} W_{ij}(h_i). \qquad (92)$$

We repeat this iteration from the procedure 3 if necessary.

Since

$$Z \propto y^{1 - \frac{1}{\zeta(P_i)}}, \qquad (93)$$

the error in y is amplified by the direct substitution when $\zeta(P_i) < 1/2$. To avoid this instability, we adopt Eq. (91), in which the new Z_i is taken between old Z_i and predicted Z_i, to update Z in the iteration.

4.4. Specific Form of $G(P)$

Formally, any kind of function is possible as $G(P)$. However, since our aim of the introduction of such a function for the formulation is to reduce errors induced by huge pressure jumps, it is natural to select a function which depends weakly on the value of pressure. Here, we consider the following power law form:

$$y_i = P_i^\zeta, \qquad (94)$$

where ζ is a constant value less than unity. This selection makes $\zeta(P)$ a constant value ζ. For instance, when we choose $\zeta = 0.1$, the pressure contrast with the ten orders of magnitude is reduced that with an orders of magnitude. It is worth noting that $\zeta = 1$ is the special case in which the equations are reduced to those we obtained in §3 and the Ritchie & Thomas formulation. We expect that this formulation would improve behaviors under strong shocks.

It is also noted that $\zeta = 0$ is the other special case in which the equations solve the evolution of volume elements which is independent of pressure gradient. The fundamental equation of this SPH is

$$1 = \sum_j V_j W_{ij}(h_i). \qquad (95)$$

The equations of energy and motion can be drawn in the same way we have shown in this paper. This formulation keeps important properties of the generalized DISPH that it is density independent formulation and it reduces the problem due to pressure jump around strong shocks. Further investigation of this formulation is beyond the scope of this paper. We will study this formulation elsewhere.

5. NUMERICAL EXPERIMENTS

In this section, we show the results of several standard tests for fluid schemes, for both the standard SPH and our new SPH. In §5.1, we describe our numerical code briefly. In §5.2, we show the results of the shock tube tests. Then we show the evolution of system which is initially in hydrostatic equilibrium in §5.3. In §5.4 and §5.5, tests for two important fluid instabilities are carried out. Point like explosion tests are shown in §5.6. In §5.7, we show the results of the blob tests which was first proposed by Agertz et al. (2007). As an extra test, we describe the mixing of a two phase fluid with a solid body like spoon which is found in Springel (2010a). In all tests, our new SPH shows much better result compared to that of the standard SPH.

5.1. Numerical Method

We used ASURA, a parallel N-body/SPH code, as the framework of current numerical experiments. ASURA adopts the leap-frog method for the time-integration. For simplicity, we used the shared steps with variable time-steps. The time-step is given by

$$dt = \min_i dt_i, \qquad (96)$$

where

$$dt_i = C_{\mathrm{CFL}} \frac{2h_i}{\max_j v_i^{\mathrm{sig}}}, \qquad (97)$$

and $C_{\mathrm{CFL}} = 0.3$.

For the standard SPH, we first evaluated the densities and kernel sizes of particles using Eq. 16 and iteration. Then, we calculated the pressure gradient and the time-derivative of the internal energy using Eqs. 17 and 18. In DISPH, we computed q using Eq. 27 and kernel sizes first, and then we calculated the pressure gradient and the time derivative of the internal energy using Eqs. 39 and 33. For most of tests, we used a special DISPH which adopt q as a fundamental value. We investigated the advantages of the generalized DISPH and the grad-h term in the strong shock test in §5.6. We used Eq. 46 as the artificial viscosity term in both cases and we adopted $\alpha = 1$ as a fiducial value. In the loop where we compute q, we also compute smoothed mass densities since they are used in the calculation of the artificial viscosity term. The Balsara switch was also applied. To avoid the pairing instability, we used a first derivative of the kernel which has a cuspy core (Thomas & Couchman 1992). Note that this modification leads to an inconsistent sound speed and other quantities within $s = |\boldsymbol{r} - \boldsymbol{r}'|/h < 2/3$ (See footnote 8 in Price 2012). The essential solution is to use kernels which do not show the pairing instability, for instance, the kernel proposed by Read et al. (2010) and Wendland kernels (Dehnen & Aly 2012).

The kernel size of each particle is determine to keep the number of neighbor particles within the range of 32 ± 2. As an exception, in the one-dimensional tests shown in §5.2, the kernel size is evaluated by

$$h = \eta \left(\frac{m}{\rho} \right), \qquad (98)$$

where $\eta = 1.2$ for the Sod's shock tube tests and $\eta = 2.4$ for the strong shock tube tests. For DISPH, we used the smoothed density for the evaluation of the kernel size.

5.2. Shock Tube Tests

The Sod shock tube (Sod 1978) is the most basic test for numerical schemes for compressible fluid. This test shows the shock capturing ability of schemes. In SPH, not only the profile of the shock front but also the behavior of the contact discontinuity is important. Here, we show the results of one- and three-dimensional shock tube tests.

The setup is as follows. We prepared the periodic domain of $-1 \leq x < 1$ for the one-dimensional tests and $-1 \leq x < 1$, $-1/16 \leq y < 1/16$, and $-1/16 \leq z < 1/16$ for the three dimensional tests. The initial condition is given by

$$\begin{cases} \rho = 1, P = 1, v = 0, & x < 0, \\ \rho = 0.25, P = 0.1795, v = 0, & x \geq 0. \end{cases} \qquad (99)$$

To express this initial condition, we use equal-mass particles and place 800 and 200 particles in the left and right domains, respectively, regularly in the one-dimensional tests. In three dimensional tests, we place 40000 and 10000 particles in the left and right domains, respectively, and a glass-like particle distribution was used. We set $\gamma = 1.4$ and gave the internal energy to each particle to ensure the given P.

In addition to the Sod shock tube, we performed a one-dimensional strong shock test. The initial condition for this test is given by

$$\begin{cases} \rho = 1, P = 1000, v = 0, & x < 0, \\ \rho = 1, P = 0.01, v = 0, & x \geq 0. \end{cases} \qquad (100)$$

We use 1000 equal-mass particles in the computational domain of $-1 \leq x < 1$ with the equal separation.

Figure 2 shows the results of the one-dimensional shock tube tests with the standard SPH and DISPH. The density (upper row) and pressure (bottom row) of each particle are plotted by circles. The red curves represent the analytic solutions.

The standard SPH reproduces the analytic solution of the density distribution well. The shock front is resolved by ~ 7 particles. The jump of the density at the contact discontinuity is resolved by a similar number of particles. The pressure shows large variations near the contact discontinuity, though it should be constant. Since Eq. 9 of the standard SPH contains a large error near the contact discontinuity, in order to achieve zero acceleration, pressures of particles must have large variations. This result is the same as the results of previous works with the standard SPH (e.g., Springel 2005; Price 2008).

In DISPH, unlike the case of the standard SPH, the pressure around the contact discontinuity does not show
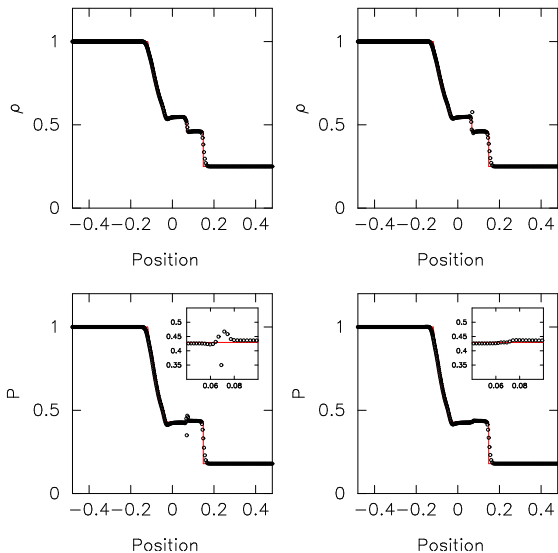
Figure 2. The results of the one dimensional shock tube tests for the standard SPH and DISPH at $t = 0.1$. Density (upper row) and pressure (bottom row) are shown. Circles indicate the physical quantities of each SPH particle, while red curves represent the analytic solutions. Insets in the pressure panels are the close-up views around the contact discontinuity.
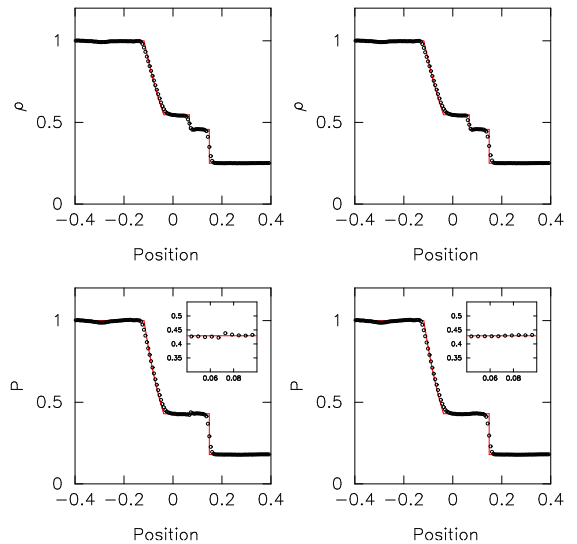

Figure 3. The results of the three dimensional shock tube tests for the standard SPH and DISPH at $t = 0.1$. Density (upper row) and pressure (bottom row) are shown. Circles indicate the averaged physical quantities of SPH particles, while red curves represent the analytic solutions.

a large jump. The reason is simply that the energy density is used instead of the mass density. The energy density is constant at the contact discontinuity. The reason why there is a small change in the pressure is that the particle separation changes at the contact discontinuity. As we showed in figure 1, our new SPH still has small error in the pressure, due to the finite number of particles in the kernel. This error caused the change in the pressure in figure 2.

The results of the three dimensional shock tube tests for the standard SPH and our SPH are shown in figure 3. In this figure, the circles represent average values of particles in bins with the width of the mean particle separation at the high density part. Again, we can see a variation in the pressure around the contact discontinuity in the case of the standard SPH. In the case of our SPH, there is no such variation.

Figure 4 shows the results of the strong shock tube tests for the standard SPH and DISPH. The shock front and the contact discontinuity in the density distribution is well reproduced in the both cases. In this extreme test, both runs show jumps in the pressure distribution around the contact discontinuity. The absolute value of the pressure jump in DISPH is much smaller than that in the standard SPH. The jump found in the pressure in our SPH is caused by the asymmetry in the particle distribution (see §3.6). Overall, DISPH can handle such a strong shock problem, even when a very large pressure jump exists initially. This result is quite reassuring. In DISPH, it is assumed that pressure is smooth, which is not a valid assumption at the shock front. Thus, it could fail to capture very strong shocks. The result shown in figure 4 shows that is not the case and new SPH can handle very strong shocks.

5.3. Hydrostatic Equilibrium Tests

As is shown in §2, in the standard SPH, particles feel *unphysical repulsive force* at the interface of the contact
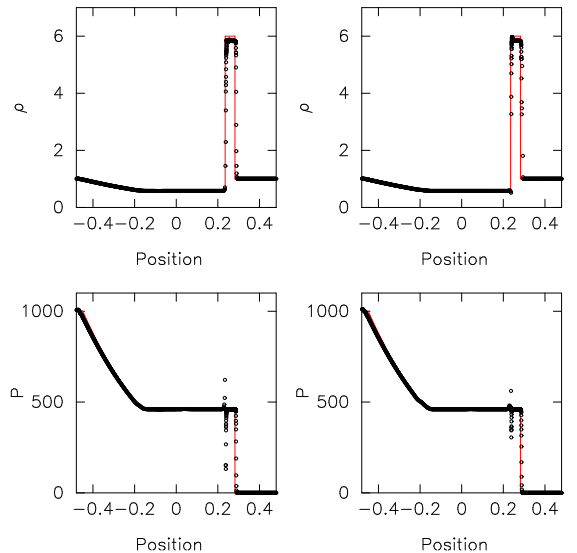
Figure 4. The same as figure 2, but for the strong shock tube tests at $t = 0.012$.

discontinuity. Therefore, in order to establish the hydrostatic equilibrium, the distance between particles at the different sides of the contact discontinuity must become larger than the "true" value. What is the consequence of this repulsive force? Here, we show the result of a simple test which helps us to understand the problem of the unphysical repulsive force. Similar test has been used in Heß & Springel (2010).

We follow the evolution of two fluids with different values of density, but with the same pressure. We performed two-dimensional tests. The computational domain is a square of the unit size, $0 \leq x < 1$ and $0 \leq y < 1$, with a periodic boundary condition. Initial conditions are

$$\rho = \begin{cases} 4 & 0.25 \leq x \leq 0.75 \text{ and } 0.25 \leq y \leq 0.75, \\ 1 & \text{otherwise,} \end{cases} \quad (101)$$

$$P = 2.5, \qquad\qquad\qquad (102)$$

$$\gamma = 5/3. \qquad\qquad\qquad (103)$$

We tried two different realizations. In the first one, the particle mass is the same for the entire computational region. Thus, the inter-particle distance is smaller in the high density region. In the second one, particles in the high density region is four times more massive than particles in the low-density region. In both cases, particles are initially in a regular grid. For the equal-mass case, the number of particles in the dense region is 4096 and that in the ambient is 3072. For the equal-separation cases, those are 1024 and 3072, respectively. Initial velocities of particles were set to zero. Since the system is initially in the hydrostatic equilibrium, particles should not move, except for small local adjustments.

Figure 5 shows the time evolution up to $t = 8$. There is a clear difference between the result of the standard SPH and that of DISPH. With the standard SPH, the high-density region, which initially has a square shape, quickly becomes rounder and almost completely circular by $t = 8$. We can understand this unphysical rounding as follows. As we stated in §2 and §3.6, unphysical repulsive force between particles operates at the contact discontinuity. We can see the effect of this force in the development of the gap of the distribution of particles near the boundary of two fluids. Because of this gap, the bulk of the system is slightly compressed. The system seeks to achieve the energy minimum, by minimizing the surface area of the contact discontinuity. Thus, the high-density region evolves to a circular shape, which minimizes the length of the boundary. In other words, the repulsive force effectively adds the "surface tension".

DISPH gives a far better solution, as we can see in the lower two rows of figure 5. The overall square shape remains there till the end of the simulation in the equal-mass case. The result of the unequal-mass case is even better. The equation of motion of DISPH eliminates the unphysical surface tension completely.

Figure 6 shows the final state of the two-fluid system with the density contrast of 64. Our SPH handles the system without any problem (right panel). On the other hand, in the calculation with the standard SPH, a wide and empty ring structure is formed between two fluids.

5.4. Kelvin-Helmholtz Instability Tests

After the work by Agertz et al. (2007) which demonstrated clearly that the standard SPH cannot deal with the Kelvin-Helmholtz instability correctly, many researchers proposed modifications of SPH to solve the problem (see §1). In this section, we investigate how DISPH handles the Kelvin-Helmholtz instability.

We prepared a two-dimensional computational domain, $0 \le x < 1$ and $0 \le y < 1$. The periodic boundary condition was used. The initial density is

$$\rho = \begin{cases} 1 (\equiv \rho_l) & 0 \le y < 0.25, \ 0.75 \le y < 1, \\ 2 (\equiv \rho_h) & 0.25 \le y < 0.75. \end{cases} \quad (104)$$

We used equal-mass particles. The numbers of particles in the high and low dense regions are 131072 and 65522, respectively. We set $P = 2.5$ and $\gamma = 5/3$. The high and low density regions had the initial velocities of $v_{x,h} = 0.5$ and $v_{x,l} = -0.5$ in the x direction, respectively.

We have used $N_{\rm nb} = 32 \pm 2$ as the neighbor number. This value might seem a bit large, but we found it guarantees the good sampling of the particles in the low-density region at the interface. When we used $N_{\rm nb} = 16 \pm 2$, the variation of the pressure at the interface becomes too large. For the artificial viscosity, we used $\alpha = 1$ with the Balsara switch.

We added a small velocity perturbation to the particles near the interfaces, following Price (2008). The velocity perturbation in the y direction is as follows:

$$\Delta v_y = \begin{cases} A \sin[-2\pi(x+0.5)/\lambda], & |y - 0.25| < 0.025 \\ A \sin[2\pi(x+0.5)/\lambda], & |y - 0.75| < 0.025, \end{cases}$$
$$(105)$$

where $\lambda = 1/6$ and $A = 0.025$.

The time-scale of the growth of the Kelvin-Helmholtz instability is

$$\tau_{\rm kh} = \frac{\lambda(\rho_h + \rho_l)}{\sqrt{\rho_h \rho_l} |v_{x,h} - v_{x,l}|}. \qquad (106)$$

For our test setup, $\tau_{\rm kh} = 0.35$. We followed the evolution up to $t = 8\tau_{\rm kh}$.

The results are shown in figure 7. The difference between two results is clear. In the run with the standard SPH, perturbations grow till $t = \tau_{\rm kh}$, but the unphysical surface tension inhibited the growth of roll-like structures. The stretched high-density fluids break apart ($t = 4\tau_{\rm kh}$) and form blobs ($t = 8\tau_{\rm kh}$). This evolution is completely different from those obtained by Euler codes (e.g., Agertz et al. 2007). On the other hand, DISPH shows a very good result which is comparable to those with Euler codes and with SPH codes adopting the Ritchie & Thomas (2001) equation of motion or the artificial conductivity (see Price 2008). Price (2008) reported that the instability grew but did not develop prominently when the Ritchie & Thomas formulation was used. He argued that this failure was because of noise when the Ritchie & Thomas formulation was used and the low resolution (See figure 5 in his paper). In our test, we observed extended Kelvin-Helmholtz instabilities with the resolution same as that used in Price (2008). When we turned off the Balsara switch, instabilities did not developed, and we obtained the result similar to Price's result. The use of the Balsara switch is important for such a simulation of shear flows.

Figure 8 shows the cross section of the pressure distribution along the y-axis. We can see that a very large pressure jump exists around the contact interfaces, in the case of the standard SPH. The surface tension at the interface of the two fluids prevents the normal growth of the Kelvin-Helmholtz instability. On the other hand, there is no such jump in the case of DISPH. Since the pressure and particle distribution is well-behaved at the interface, the growth of the Kelvin-Helmholtz instability is not suppressed.

5.5. Rayleigh-Taylor Instability Tests

Abel (2011) demonstrated that the standard SPH cannot follow the development of the Rayleigh-Taylor instability correctly. We show the result with our SPH as well as that with the standard SPH.

The initial setup is as follows. We prepared the two dimensional computational domain of $0 \le x < 1$ and
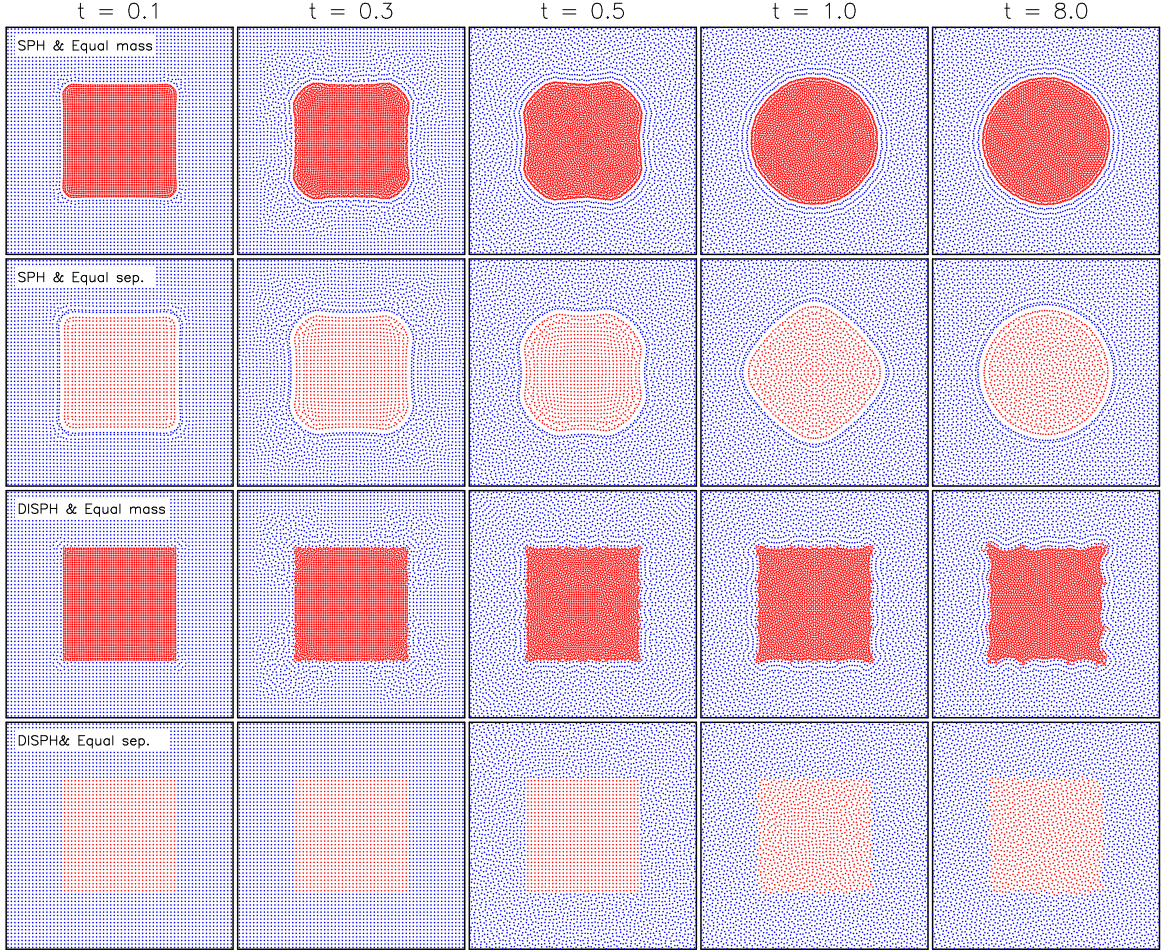
Figure 5. Snapshots of a two-fluid system at $t = 0.1$, 0.3, 0.5, 1 and 8. The red and blue points indicate the positions of particles with $\rho = 4$ and $\rho = 1$, respectively. The upper two rows are the results of the standard SPH, while the lower two rows are those of DISPH. The first and third rows show the results of the equal-mass cases, whereas the second and fourth rows show those of the equal separation and unequal mass cases.
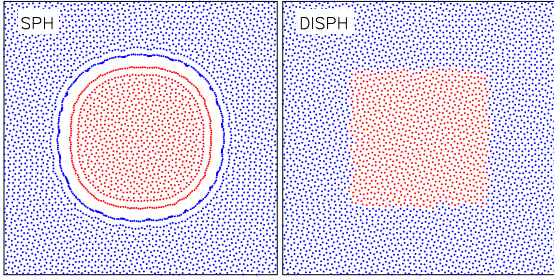
Figure 6. The final state ($t = 8$) of a two fluid system with the density contrast of 64. The red and blue points are the positions of particles with $\rho = 64$ and 1, respectively. The particle separation is constant and the particle mass difference is 1:64.

$0 \leq y < 1$. We placed two fluids separated at $y = 0.5$. The density just above (below) the interface was set to $\rho_h \equiv 2$ ($\rho_l \equiv 1$). These two fluids were initially in the hydrostatic equilibrium. Further, we assumed that each fluid was initially isentropic. The density distributions of these fluids in the vertical direction are given by

$$\rho = \begin{cases} \rho_l \left[1 + \frac{\gamma-1}{\gamma} \frac{\rho_l g(y-0.5)}{P_0}\right]^{\frac{1}{\gamma-1}} & y < 0.5, \\ \rho_h \left[1 + \frac{\gamma-1}{\gamma} \frac{\rho_h g(y-0.5)}{P_0}\right]^{\frac{1}{\gamma-1}} & y \geq 0.5, \end{cases} \quad (107)$$

where $g = -0.5$ is the gravitational constant, $P_0 = 10/7$ is the value of pressure at the interface, and $\gamma = 1.4$. The initial density and entropy profiles are shown in figure 9. To ensure the initial density distribution given by Eq. (107), we first placed equal-mass particles on the regular grid with the separation of $1/512$. Then, we adjusted the vertical separation of each particle set having the same y to reproduce the density distribution. The particle mass was set to 5.7×10^{-6} and the total number of particles was 247296. The periodic boundary condition was imposed on the x direction. Particles with $y < 0.1$ and $y > 0.9$ were fixed at the initial positions and they were not allow to change their internal energy.

The velocity perturbation in the vertical direction was added as the seed of the instabilities. We carried out runs with two kinds of the seed. For the first test, we added the velocity perturbation to particles in the range of $0.3 < y < 0.7$, and the form of the perturbation is

$$\Delta v_y(x, y) = \delta_{vy}[1 + \cos(4\pi x)]\{1 + \cos[5\pi(y - 0.5)]\}. \quad (108)$$

We set $\delta_{vy} = 0.025$. For the second test, we added the
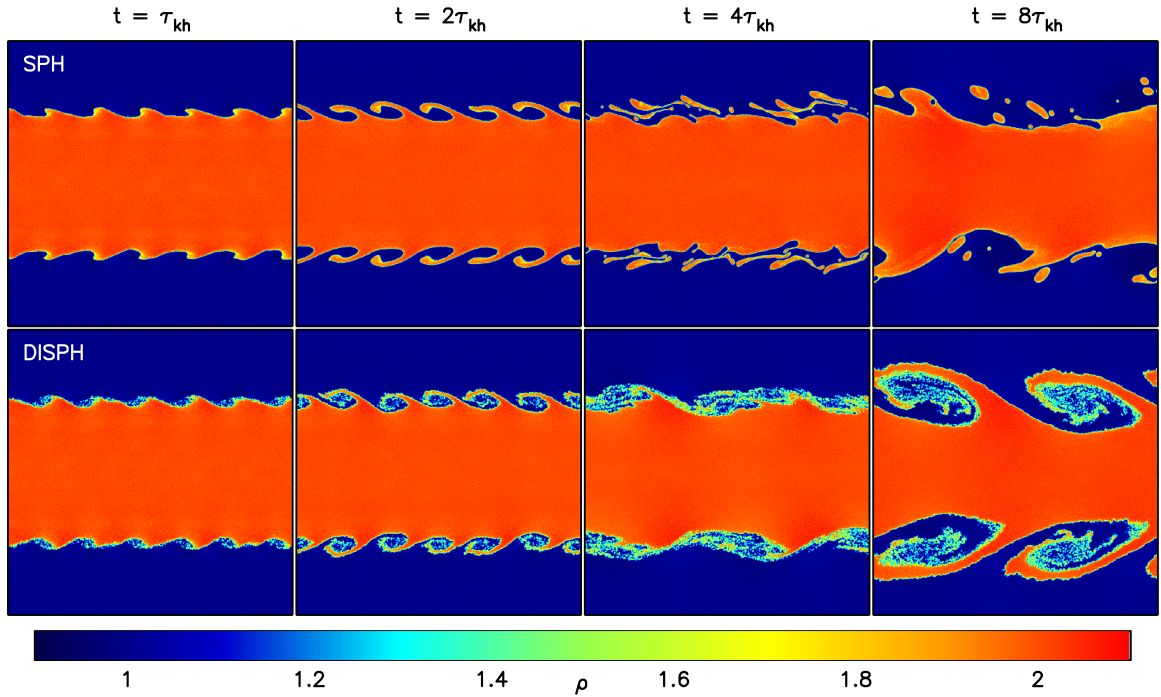
Figure 7. The density maps from the two dimensional shear flow test at $t = 1, 2, 4$ and 8 τ_{kh}. The upper panels show the results of the standard SPH, while the bottom panels show those of DISPH. The color code of the density is given at the bottom.
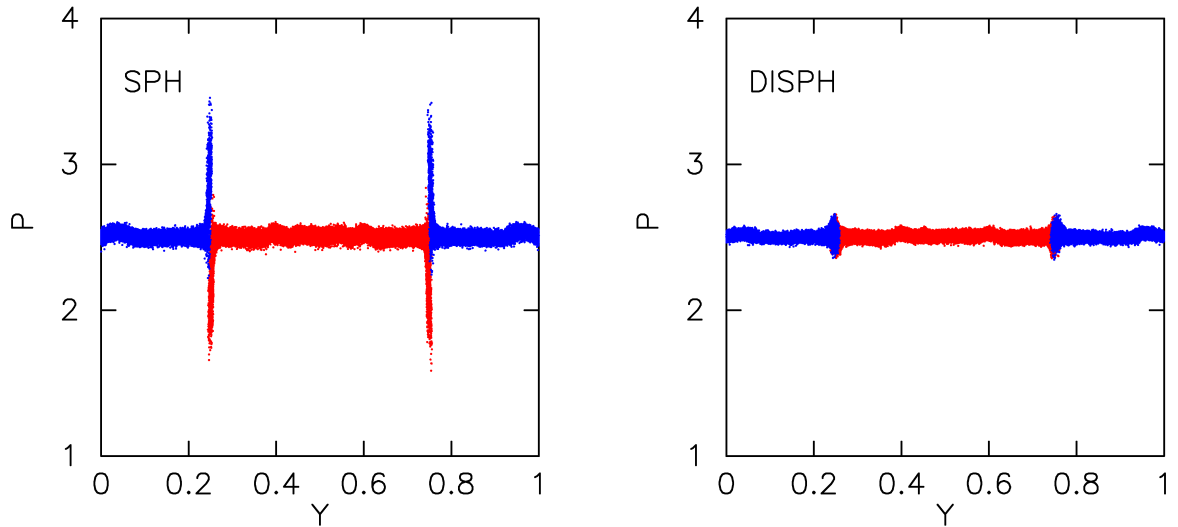
Figure 8. Pressure of each particle along the y direction at $t = 0.4$ τ_{kh}. The left panel shows the result of the standard SPH, whereas the right panel shows that of DISPH. Particles initially in the high- (low-) density region are expressed with red (blue) points.

velocity perturbation of the form:

$$\Delta v_y(x, y) = \sum_{j=20}^{40} a_j \frac{n_j}{k_j} \cos(k_j x) \exp(-0.05 k_j |y - 0.5|),$$

$$(109)$$

and

$$n_j^2 = k_j |g| \left(\frac{\rho_h - \rho_l}{\rho_h + \rho_l} \right), \qquad (110)$$

where n_j is the linear growth rate of the Rayleigh-Taylor instability, and $k_j = j\pi/L(\equiv 1)$ is the wave number of the perturbation. The amplitude of each mode, a_j, was

drawn from a Gaussian distribution with the variance of unity at random. This initial velocity perturbation is based on Youngs (1984) with slight modifications. Velocities of the particles outside the perturbed region was set to zero. We call these two tests single-mode and multi-mode tests, respectively.

In figure 10, the growth of the Rayleigh-Taylor instability in the case of the single-mode test is shown. The Rayleigh-Taylor instability develops in calculations with both of the standard SPH and our SPH, but the structures of them are quite different. The unphysical surface tension of the standard SPH again prevents the development of the fine structures on the surface of the Rayleigh-
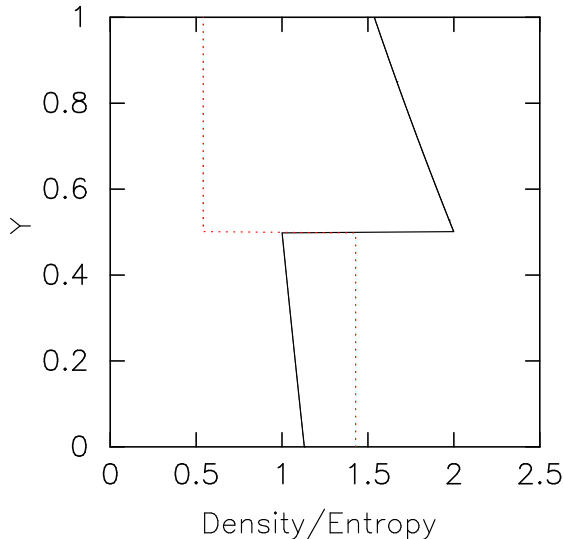
Figure 9. Initial distributions of density and entropy in the vertical direction. Solid and dotted curves indicate density and entropy, respectively.

Taylor fingers. Thus, the result looks quite different from those obtained with Euler schemes. On the other hand, in the calculation with our SPH, the overall evolution of the Rayleigh-Taylor instability in our SPH shows excellent agreement with those with Euler schemes and the moving mesh scheme (see Springel 2010a).

Figure 11 shows the growth of the Rayleigh-Taylor instability with the multi-mode perturbations with the standard SPH and DISPH. The global phase mixing of fluids can be seen in the result with our SPH. On the other hand, due to the unphysical surface tension, the mixing is significantly suppressed in that of the standard SPH. The distribution of two fluids looks like a mixture of oil and water.

5.6. *Point Like Explosion Tests*

In this section we describe the results of the test calculations for a point-like explosion.

We prepared a three-dimensional computational domain of $0 \leq x, y, z < 1$ with a periodic boundary condition. Then, we placed 64^3 equal-mass particles in that domain and made a glass like distribution. The particle mass is $1/64^3$. Thus the initial density was unity. The explosion energy was injected to the center of the domain. The total thermal energy of unity was distributed following the shape of the SPH kernel with the kernel size in which N_s particles were included. Here, we tested $N_s = 32$ and $N_s = 256$. After that, we added the thermal energy of 10^{-6} of the particle with the maximum energy to all particles. This energy difference between the hot region and the ambient corresponds to the supernova explosion in a cold cloud. In this test, we adopted the viscosity parameter $\alpha = 3$.

We compared results of three schemes, *i.e.*, the standard SPH and our SPH with q and $y = P^\zeta$. For DISPH with $y = P^\zeta$, we adopted $\zeta = 0.1$ and the three iterations to determine Z in each time-step. We investigated the effects of the grad-h term, the adopted value of N_s, and the use of the density derived from EOS for the artificial viscosity term. The equations of motion and energy with

the grad-h term for the standard SPH are Eqs. (25) and (22) in Springel (2010b), while those for our SPH using q are Eqs. (61) and (68). For the generalized DISPH, we used Eqs. (75) and (74) for the run without the grad-h term and Eqs. (85) and (86) for the run with the grad-h term, respectively. Note that, unlike experiments in Hopkins (2013), the equations without the grad-h term we used here is an energy conserving ones, although these equations neglect the gradient of the kernel size. They are different from the case with $f_i^{\mathrm{grad}} = 1$.

Figure 12 shows the density and pressure profiles of three runs. In all runs, the grad-h term is used. From the top row, we can see that the density profiles of all runs are basically consistent to the analytic solution. When we compare these results, we find that the result of the standard SPH exhibits the smallest scatter in density. Our SPH with y shows the highest peak at the edge of the shell.

These density profiles are drawn using the smoothed density even though our schemes can obtain their intrinsic densities by using EOS. To compare to them, we prepared the density profiles of our schemes which used the density derived from EOS, *i.e.*, $\rho = mq/U$ and $\rho = my/Z$. These profiles are shown in figure 13. These profiles follow the analytic solution well. The peak of our SPH with y reaches to 3 and this value is higher than that obtained using the smoothed density.

However, the use of EOS density has several disadvantages. First, the scatter of density is larger than that obtained using the smoothed density, although the increase of the scatter is not so prominent. Second, at very early phase, the EOS density profile shows a large error. Indeed, the error in this test case, the error is several orders of magnitude at the initial step. If the radiative cooling is included and the cooling time is comparable to or shorter than the dynamical time, this may lead to wrong results. If the dynamical time is the shortest one of a system, this effect is negligible. Thus, this depends strongly on the situation. It would be safer to use the smoothed density for the evaluation of the amount of radiative cooling, because the cooling rate depends on the square of density and would be sensitive to the errors in density.

The logarithmic plots of density at the middle row in figure 12 indicate differences among runs more clearly. The result of the standard SPH shows that there is a systematic offset from the analytic solution in the central region, since it is hard to reproduce such a very less dense region using a given particle mass. The worst result is provided by DISPH with q. It has the largest scatter in density, and in addition, it shows the systematic offset in the central region. In the result of DISPH with y, we found that the density profile follows the analytic solution to much less dense region and the degree of the density scatter is less than that found in DISPH with q.

The pressure profiles are shown in the bottom row of figure 12. We can see that the standard SPH overestimates the pressure in the central, less dense region, whereas our SPH show improved pressure profiles. This behavior comes from the fact that our SPH adopts the pressure (energy density) or its power as the smoothed value of the formulation. Note however that the most
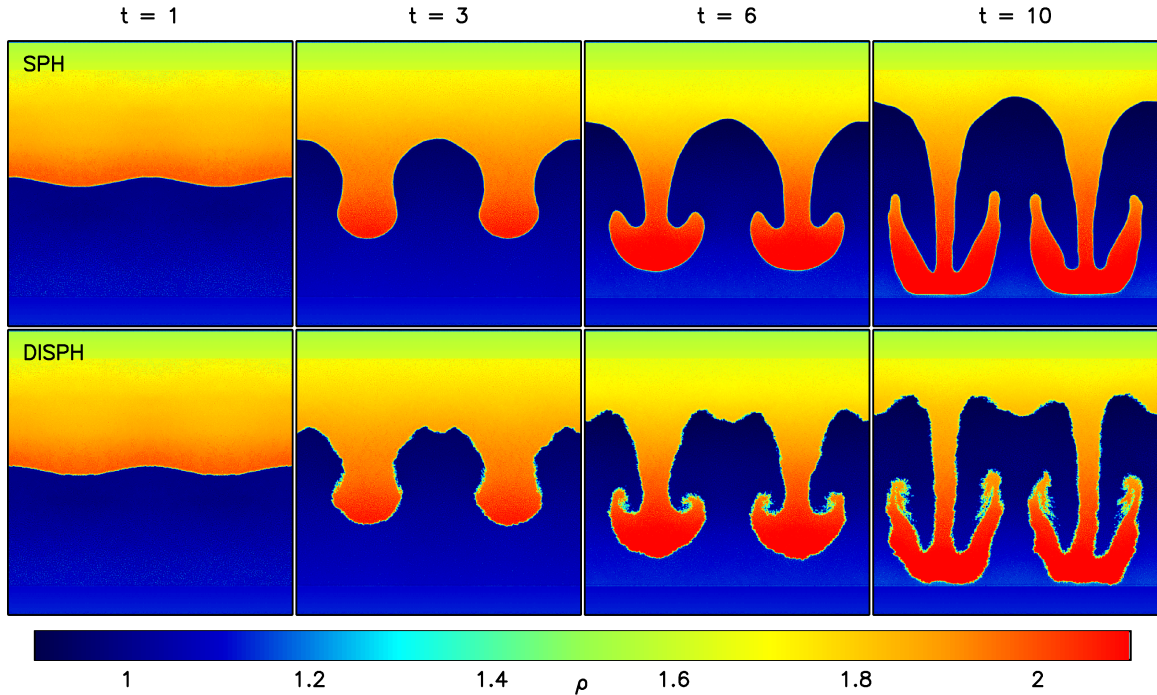
Figure 10. The density maps of the two dimensional Rayleigh-Taylor instability tests at $t = 0.5, 3, 4$ and 5. The upper panels show the results of the standard SPH, while the bottom panels show those of DISPH. The color code of the density is given at the bottom.

central particle in DISPH with q has very large error which can observed in figure 14. The pressure profile of DISPH with y follows the postshock profile of the analytic solution very well. Only this run can reproduce the peak of the pressure profile. This is because we solved the smoothed $y = P^{0.1}$ which has quite shallow gradient in the postshock region.

Figure 14, which shows the profile of the basic quantities *i.e.*, ρ, q, and y at $t = 0.01$, tells us the advantage of our SPH with $y = P^{0.1}$ over others clearly. The density distribution of the standard SPH in the postshock region has a change with several orders of magnitude due to the expansion. In our SPH with q, a decrease of q in the postshock region is much moderate. The range of y in the postshock region is less than 10%. Since the profile of the basic quantity is quite smooth, DISPH with y can follow the peak of the pressure profile very well.

The density profiles without the grad-h term are shown in figure 15. Even though the grad-h term is excluded, the standard SPH can reproduce the density profile regardless of the value of N_s. This is because the value of $\partial\rho/\partial h$ in f^{grad} is rather small in the standard SPH. When $N_s = 256$ is adopted, the profile becomes much smooth compared to that with $N_s = 32$ due to the relatively smooth, initial thermal-energy profile. On the other hand, the density profiles of our schemes with $N_s = 32$ have clear delay of the shock front. This delay can be recovered when we adopted $N_s = 256$. In our SPH with q, the gap between Eq. (59) and unity become quite large at the early phase. Even with our SPH with y, the gap in Eq. (87) and unity is non-negligible at the early phase. These gaps lead to delay of the shock front in this test. The amount of the delay in our SPH with y is smaller compared to that in our SPH with q. This means $\partial y/\partial h < \partial q/\partial h$ and is reasonable since we used

$\zeta = 0.1$.

We show the energy errors in calculations in table 1. Here, we defined the energy error as $|E(0.05) - E(0)|/E(0)$, where $E(t)$ is the summation of the kinetic and thermal energy of all particles at the time t. The energy errors in the standard SPH runs are around 10^{-4}. In the runs with $N_s = 32$, the energy error in the run with the grad-h term is an order of magnitude smaller than that without the grad-h term. However, there is no difference in the results of the runs with $N_s = 256$. The contribution of the grad-h term is small for the standard SPH runs.

The energy errors in the DISPH runs with q are comparable with those in the standard SPH runs. However, the grad-h term plays an important role for the DISPH runs with q. When the grad-h term is used, the energy error decreases even for $N_s = 256$. For the runs using DISPH with y, the energy errors are an order of magnitude larger than others, however the values are still acceptable (less than ~ 0.1 %). When we increase the iteration count from 3 to 10, the energy errors decrease by a factor of few or an order of magnitude. The results are insensitive to the use grad-h term and the adopted value of N_s in this case.

We note that the energy errors in the runs without the grad-h term is sufficiently low. This is natural since our formulation without the grad-h term is constructed to conserve energy and momentum. Hopkins (2013) pointed out that the runs with $f^{grad} = 1$ did not conserve the total energy (see figure 2 in Hopkins 2013). However, he just adopted $f^{grad} = 1$ and did not use the symmetrized kernel in his tests. Obviously, this reformulation breaks conservations of energy and momentum.

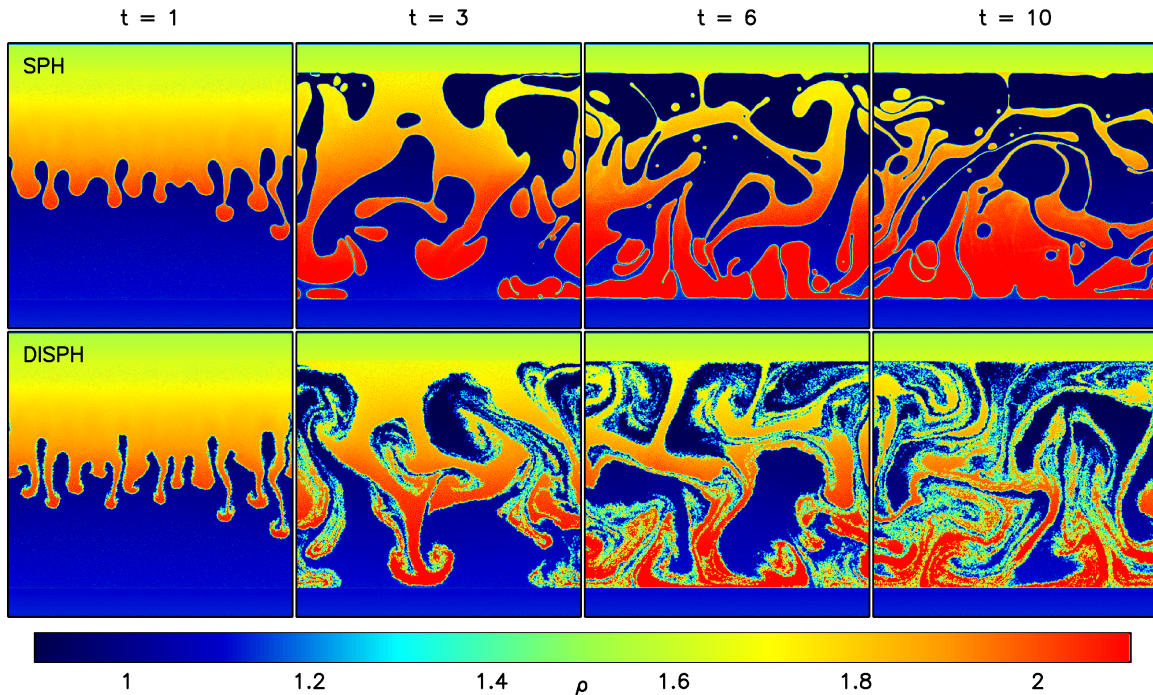Finally, we investigate the case that the density obtained by EOS is used for the evaluation of the artificial

Figure 11. The same as figure 11, but for the multi-mode perturbations.

Table 1
Energy error in the Sedov tests.

Run	Iteration	N_s	with grad-h	without grad-h
SPH	N/A	32	4.8×10^{-5}	5.3×10^{-4}
SPH	N/A	256	3.6×10^{-4}	3.4×10^{-4}
DISPH(q)	N/A	32	6.5×10^{-4}	1.5×10^{-3}
DISPH(q)	N/A	256	3.9×10^{-5}	6.2×10^{-4}
DISPH(y)	3	32	2.7×10^{-3}	6.7×10^{-3}
DISPH(y)	3	256	4.1×10^{-3}	3.5×10^{-3}
DISPH(y)	10	32	2.8×10^{-4}	1.1×10^{-3}
DISPH(y)	10	256	1.1×10^{-3}	6.7×10^{-4}

viscosity term. Instead of the smoothed mass density, we adopted $\rho = mq/U$ and $\rho = my/Z$ to evaluate ρ_{ij} in Eq. (46) for DISPH with q and y, respectively, and depicted the density profiles in figure 16. By comparing the left panels in figure 16 and the middle panels in figure 15, we can see that the use of the EOS density makes the situation much worse. The scatter of the density profile and the delay of the shock front increase. We found that the delay due to the exclusion of the grad-h term is recovered when we used $N_s = 256$. However, in this case, there is still a non-negligible delay. The error in the EOS density induced by the error in pressure profile distorted the evolution of the expanding shell. The viscosity is the quantity which relates to the inertial force. Thus, the use of the smoothed mass density in the artificial viscosity term is generally suitable and this result support this idea. Interestingly, in DISPH with y, the use of the EOS density for the artificial viscosity makes no difference.

In appendix A of Read & Hayfield (2012), they discussed the problem in the Ritchie & Thomas formulation. They showed that it could not handle the strong shock (see figure A1 in their figure). We found that the treatment of the artificial viscosity term and the exclusion of the grad-h term are keys of this problem. Careful choice of equations, the density evaluation method for the artificial viscosity term, and the energy input scale provides good results even when the SPH formulation with the smoothed pressure (energy density) is adopted.

5.7. *Blob Tests*

In this subsection, we performed the blob test proposed by Agertz et al. (2007). This test incorporates both the Kelvin-Helmholtz and Rayleigh-Taylor instabilities.

We used Read's initial condition of the blob test (Read et al. 2010; Read & Hayfield 2012) [2]. The computational domain was $0 \le x < 2000$ kpc, $0 \le y < 2000$ kpc, and $0 \le z < 6000$ kpc, and the periodic boundary condition was imposed. A cold cloud of the density $\rho_c = 3.13 \times 10^{-7}$ in the mass unit of $2.3 \times 10^5 \ M_\odot$ and the length unit of 1 kpc and temperature $T_c = 10^6$ K was centered at $(x, y, z) = (1000 \text{ kpc}, 1000 \text{ kpc}, 2000 \text{ kpc})$. The radius of this cloud was 197 kpc. This cloud was embedded in the diffuse ambient gas of which density and temperature were $\rho_a = 3.13 \times 10^{-8}$ and $T_a = 10^7$ K, respectively. The ambient gas had the velocity of $v_z = 1000$ km s^{-1}. Thus, the Mach number of the flow to the cloud was 2.7. The total number of particle for the system is 4643283. We integrated the system up to $t = 5\tau_{kh}$, where $\tau_{kh} = 2$ Gyr is the typical growth time-scale of the Kelvin-Helmholtz instability in this test (Agertz et al. 2007).

Figure 17 shows the snapshots of the cloud core. The upper and lower panels are the results with the standard SPH and DISPH, respectively. Their evolutions were quite different. The blob simulated with the standard SPH retained the single cloud structure until the

---

[2] We obtained the initial condition from the following URL: http://www-theorie.physik.uzh.ch/astrosim/code/
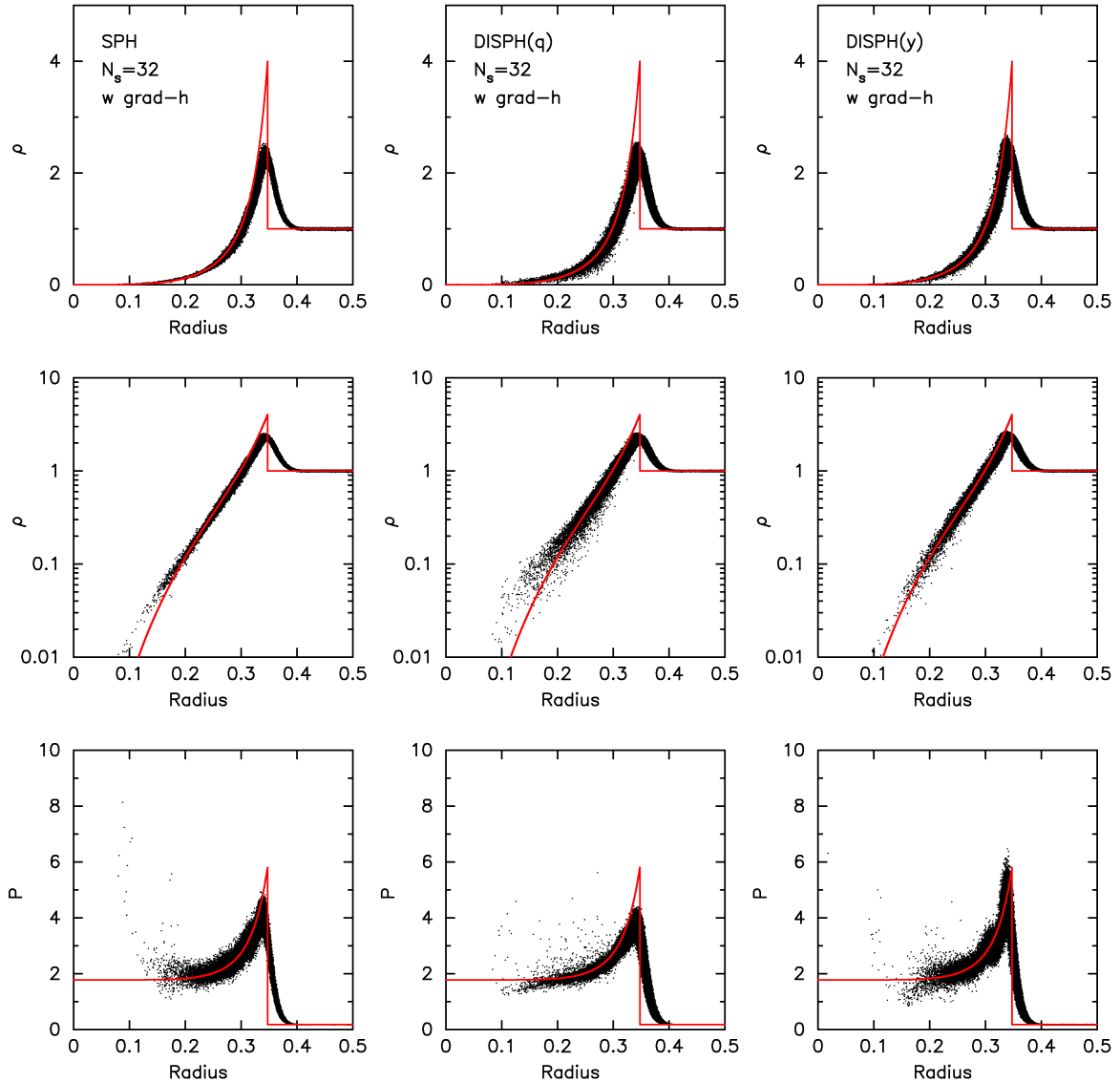
Figure 12. Density and pressure profiles of three runs using the standard SPH and DISPH with q and y at $t = 0.05$. The grad-h term is taken into account and $N_s = 32$. Dots represent the quantity of each particle. All of particles are used for plots. The smoothed density is used to depict the density profiles. Red curves are the semi-analytic solution (Sedov 1959).

late stage of the simulation. This behavior is consistent with those with the standard SPH shown in Agertz et al. (2007). In contrast, the blob surface was disrupted in the run with our SPH, due to the growth of the instabilities on the surface. The blob fragmented into several peaces and mixed eventually with the ambient gas. This behavior is similar to those obtained by Euler codes.

The evolution of the blob mass is shown in figure 18. Here we show the mass of gas with $\rho > 0.64 \, \rho_c$ and $T < 0.9 \, T_a$, following Agertz et al. (2007). At $t = 2.5 \, \tau_{kh}$, the blob mass in the run of DISPH became $\sim 10 \%$ of the initial mass. This result is consistent with the results of the Euler codes (see figure 6 in Agertz et al. 2007). The evolution of the blob mass in the standard SPH was much slower compared to that in DISPH.

5.8. *Mixing of Two Phase Fluid with Spoon*

In this subsection, we discuss the results of simulations of two fluid mixed with a solid body like a spoon.

With this test, we can see the ability of a particle-based scheme to handle fixed and moving boundary conditions. The setup of this test is similar to that in section 8.9 of Springel (2010a).

The initial setup is as follows. We prepared the two-dimensional computational domain of $-0.025 \leq x \leq 1.025$ and $-0.025 \leq y \leq 1.025$. The lower part of the domain $y < 0.6$ was the dense region with the density of 1 while the upper part of the domain $y > 0.6$ was the less-dense region with the density of 0.5. To make this density distribution, we employed the equal-mass particles of which mass is 1.87×10^{-6} and we placed them on the regular grid with the separation of $1.05/768$. Then, we doubled the vertical separation of particles in $y > 0.6$. The pressure was unity in the whole region, with $\gamma = 5/3$. Sound speeds in the dense and less-dense regions were 1.3 and 1.8 in the simulation unit, respectively. Particles which were out of the range $0 \leq x < 1$ and $0 \leq y < 1$ were fixed at the initial positions and ini-
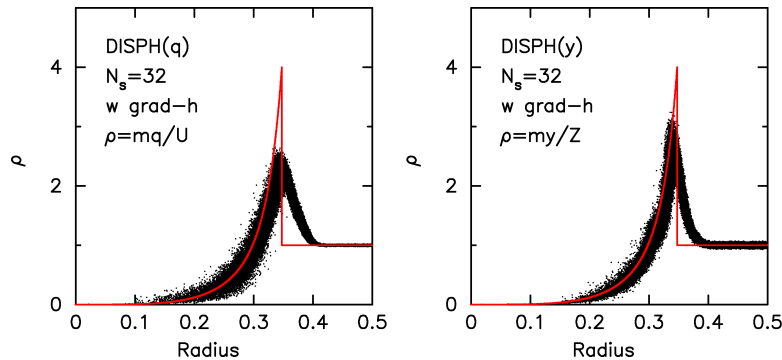
Figure 13. Density profiles of two runs using DISPH with q and y at $t = 0.05$. Here, the densities evaluated from the EOSs, $\rho = mq/U$ and $\rho = my/Z$, are used. The grad-h term is taken into account and $N_{\mathrm{s}} = 32$.
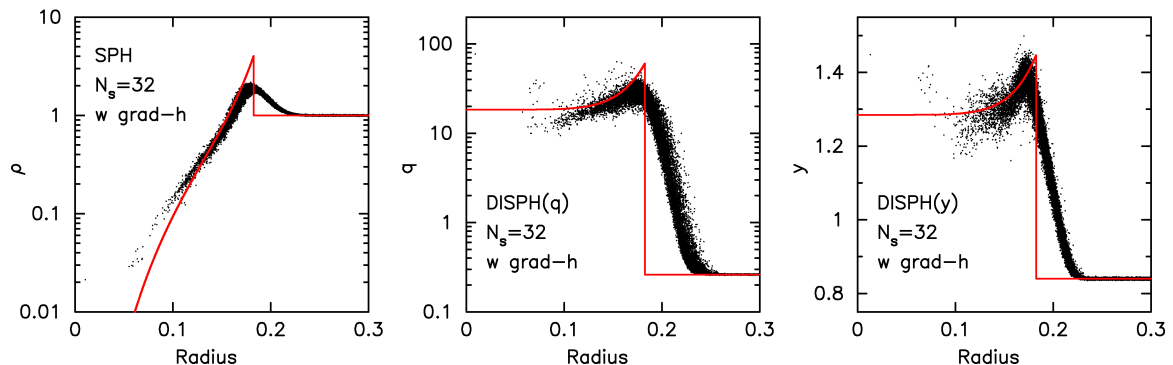
Figure 14. Comparison of fundamental quantities of three runs. From left to right, the results of the standard SPH and DISPH with q and y at $t = 0.01$ are shown. Note that the vertical axis in the right panel is linear.

tial physical quantities. These fixed particles express the fixed boundary condition. The velocity of all particles were initially set to zero. The number of particles in the dense and less-dense regions in $0 \leq x < 1$ and $0 \leq y < 1$ were 319185 and 107604, respectively, and that of the boundary particles were 41064.

We made the solid body like spoon by SPH particles. The detailed procedure is described in the appendix A. The total number of the particle consisting of the spoon was 8652. In figure 19, we show the shape of the spoon. The physical quantities and relative positions of spoon particles were kept unchanged. The spoon rotates anticlockwise around the rotation center of $(0.5, 0.5)$. The angular velocity is $2\pi/5$. We introduced a repulsive force for the interactions between fluid particles and solid body particles of the spoon so that penetrations of fluid particles to the spoon is prevented.

Figure 20 shows the snapshots of the representative epoch ($t = 0, 1.6, 3.0, 5.0, 6.5$, and 8.0) for the runs with the standard SPH and our SPH. For the run with the standard SPH, the fluid shows the clear sign of unphysical surface tension, resulting in the behavior much like that of water and oil. Although the spoon rotated the two phase fluid, the mixing of two fluids is prevented by the surface tension. Overall, the result is completely different from that obtained by the moving mesh code (see figure 39 in Springel 2010a).

The situation was drastically improved when we used DISPH. When the spoon lifted-off the dense fluid, a hammer head like structure was developed ($t = 1.6$). The fluid spilled away from the edges of the spoon and formed

eddies. These prominent structures were not observed in the run with the standard SPH, while they were observed in the moving mesh simulation (Springel 2010a).

6. SUMMARY AND DISCUSSION

In this paper, we described an alternative formulation of SPH in which the energy density (pressure), and its arbitrary function is used as the volume element instead of the mass density. In our formulation, the mass of particles is not used in the evaluation of the right-hand sides of the energy equation and the equation of motion. As a result, the large error of force estimate at the contact discontinuity, which is unavoidable with the standard SPH, disappears completely in our SPH. Our new SPH includes the Ritchie & Thomas formulation (Ritchie & Thomas 2001) as a special case. Not surprisingly, our SPH can handle contact discontinuities and the Kelvin-Helmholtz and Rayleigh-Taylor instabilities without difficulty. The behavior of the shock in DISPH is essentially the same as that in the standard SPH. Since the equations used in our SPH are almost identical to those of in the standard SPH except that a function of energy density (pressure) is used in place of mass density ρ. Modification of existing SPH code to use our scheme is simple and straightforward. In particular, there is no increase in the calculation cost at least for the case of $G(P) = P$. Equations which are not derived in this paper, such as the diffusion equation (Brookshaw 1985), can be derived easily.

Price (2008) improved the treatment of the Kelvin-Helmholtz instability of the standard SPH, by applying
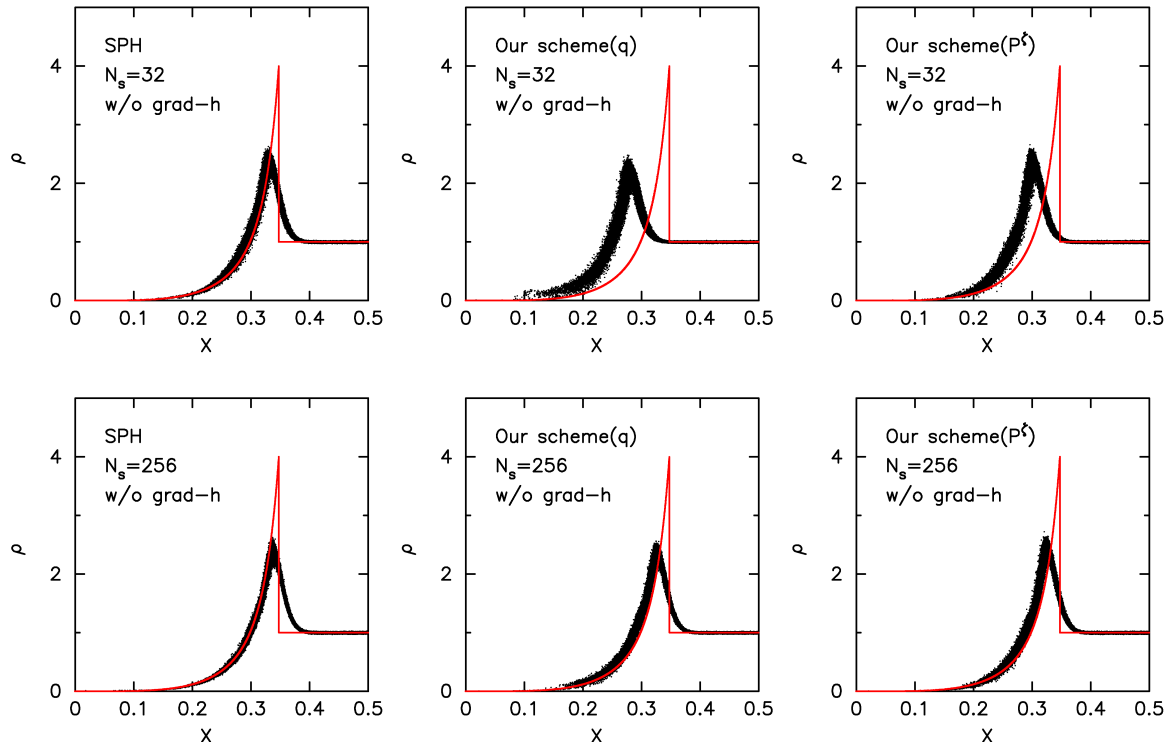
Figure 15. Effects of the grad-h term and the adopted value of $N_{\rm s}$. The top row shows density profiles without the grad-h term and $N_{\rm s} = 32$, while bottom row exhibits those without the grad-h term and $N_{\rm s} = 256$. The smoothed "mass" density is used to draw these density profiles. These profiles are obtained from snapshots at $t = 0.05$.

artificial conductivity at the contact discontinuity. Unlike the artificial viscosity, artificial conductivity introduces the dissipation not in the original set of equation. Our SPH does not need such additional dissipation, and thus the contact discontinuity is kept sharp.

One might think our result contradicts with the requirement that all quantities in SPH must be smooth (Monaghan 1997). However, it is obvious that in our SPH, all quantities in the right-hand side of the equations are smooth. Thus, our results does not contradict with Monaghan's requirement.

In this paper,we discuss the treatment of ideal gas only. We are currently working on the extension to non-ideal fluid, and the result will be given in the forthcoming paper.

APPENDIX

SETUP OF THE SOLID BODY LIKE SPOON

Here, we describe the procedure to make the spoon which was used in §5.8. To express the spoon in the fluid simulation, we first chose particles in a region of which shape is an arcuate with smooth edges. Particles in the region evolves like a solid body. We enforced that relative positions and other physical quantities of particles consisting of the spoon were kept unchanged during the simulations. To avoid the penetration of fluid particles to the spoon, we added an repulsive force which acted on the fluid particles. In below, we explain these in detail.

As shown in figure 21, we combined arcs of four circles to determine the boundary of the spoon. We picked up a ringed region which is located between two circles ($C1$ and $C2$):

$$(x - 0.75)^2 + (y - 0.7)^2 = (0.19)^2, \tag{A1}$$

$$(x - 0.75)^2 + (y - 0.7)^2 = (0.21)^2. \tag{A2}$$

Then, we cut the ringed region and made edges by putting two small circles, $C3$ and $C4$, which contact to the circles $C1$ and $C2$. The centers of two small circles are $(x_{\rm l}, y_{\rm l}) = (0.66, 0.52)$ and $(x_{\rm r}, y_{\rm r}) = (0.84, 0.52)$, respectively. Their radii are 0.01. The right (left) side of $C3$ ($C4$) makes the smooth edge.

The particle found in the enclosed region was selected and converted them into four smaller SPH particles conserving the center of mass with the separation of one-half of the original particle separation. The total number of the spoon
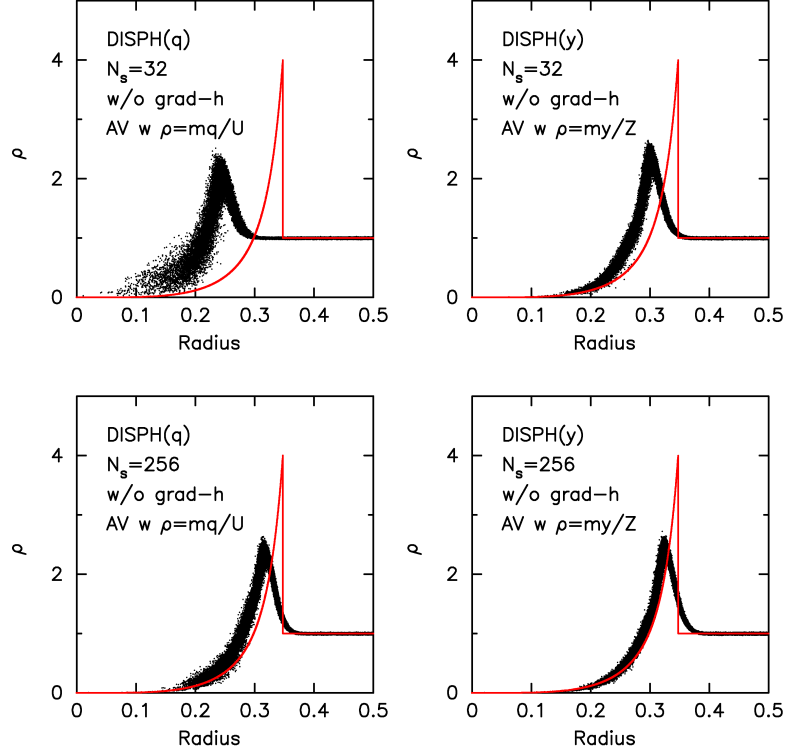
Figure 16. Density profiles for DISPH with q and y at $t = 0.05$. $\rho = mq/U$ and $\rho = my/Z$ is used to evaluate ρ_{ij} in the artificial viscosity term in the run of DISPH with q and y, respectively.
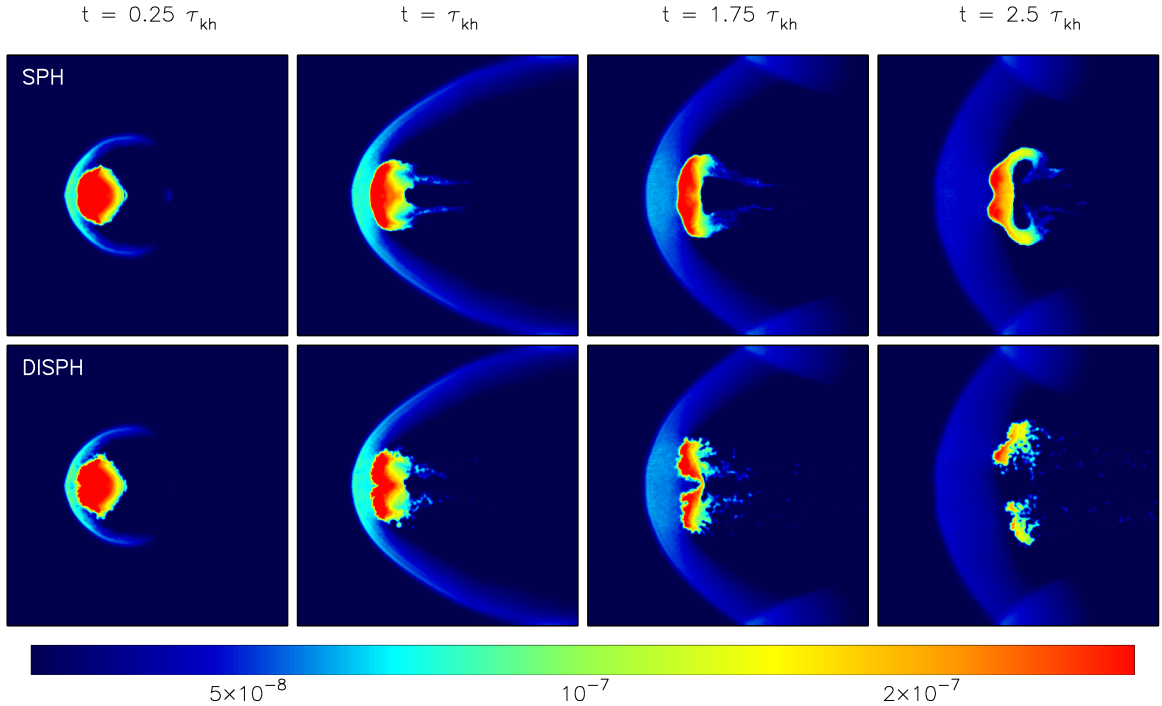

Figure 17. The density maps at $t = 0.25$, 1.0, 1.75 and 2.5 τ_{kh}. The upper and lower panels show the results with the standard SPH and DISPH, respectively. The color code of the density is given at the bottom.

particle was 6608. The spoon rotated the anti-clockwise around the rotation center of $(0.5, 0.5)$ and the angular velocity of $2\pi/5$.

The spoon faced strong pressure from the fluid particles. When we only considered the hydrodynamical force from the particles consisting the spoon, a little but non-negligible amount of fluid particles penetrated through the spoon.
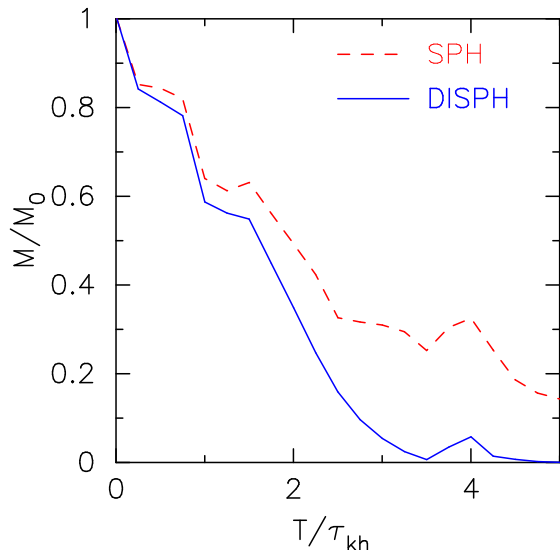
Figure 18. The evolution of the blob mass up to $t = 5 \tau_{\rm kh}$.
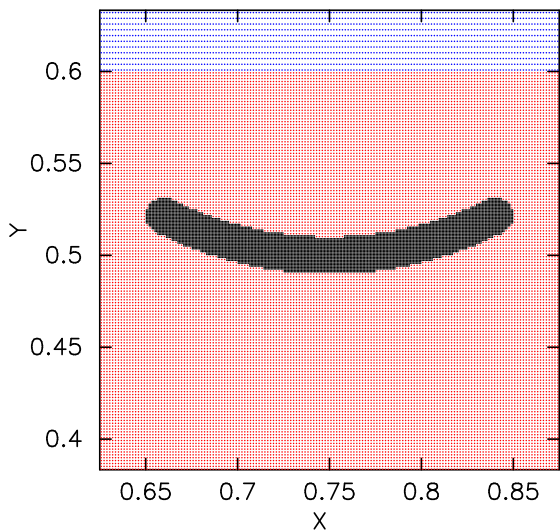
Figure 19. The two-dimensional structure of the spoon expressed by SPH particles. Black particles comprise the spoon. Red and blue particles are the fluid particles for high and low densities, respectively.

We, thus, introduced a repulsive force for the interactions between fluid particles and spoon particles. In Monaghan (1994), the Lenard-Jones potential was used for interactions between boundary particles and fluid particles. Here we choice more simple one. The form of the repulsive force between particle i and j, $\boldsymbol{F}_{ij}^{\rm rep}$, is the same as the gravitational force with the Plummer potential:

$$\boldsymbol{F}_{ij}^{\rm rep} = C \frac{m_i m_j}{|r_{ij}^2 + \epsilon_{\rm soft}^2|^{3/2}} \boldsymbol{r}_{ij}, \tag{A3}$$

where $\epsilon_{\rm soft}$ is the softening length of the repulsive force and is set to $2h$ of the spoon particles. We chose $C = 100$.

REFERENCES

Abel, T. 2011, MNRAS, 413, 271
Agertz, O., et al. 2007, MNRAS, 380, 963
Balsara, D. S. 1995, Journal of Computational Physics, 121, 357
Brookshaw, L. 1985, Proceedings of the Astronomical Society of Australia, 6, 207
Dehnen, W., & Aly, H. 2012, ArXiv e-prints
García-Senz, D., Cabezón, R. M., & Escartín, J. A. 2012, A&A, 538, A9
Gingold, R. A., & Monaghan, J. J. 1977, MNRAS, 181, 375

Hernquist, L., & Katz, N. 1989, ApJS, 70, 419
Heß, S., & Springel, V. 2010, MNRAS, 406, 2289
Hopkins, P. F. 2013, MNRAS, 428, 2840
Lattanzio, J. C., Monaghan, J. J., Pongracic, H., & Schwarz, M. P. 1985, MNRAS, 215, 125
Liu, G. R., & Liu, M. B. 2003, Smoothed particle hydrodynamics: a meshfree particle method (World Scientific Publishing Company)
Lucy, L. B. 1977, AJ, 82, 1013
Monaghan, J. J. 1992, ARA&A, 30, 543
—. 1994, Journal of Computational Physics, 110, 399
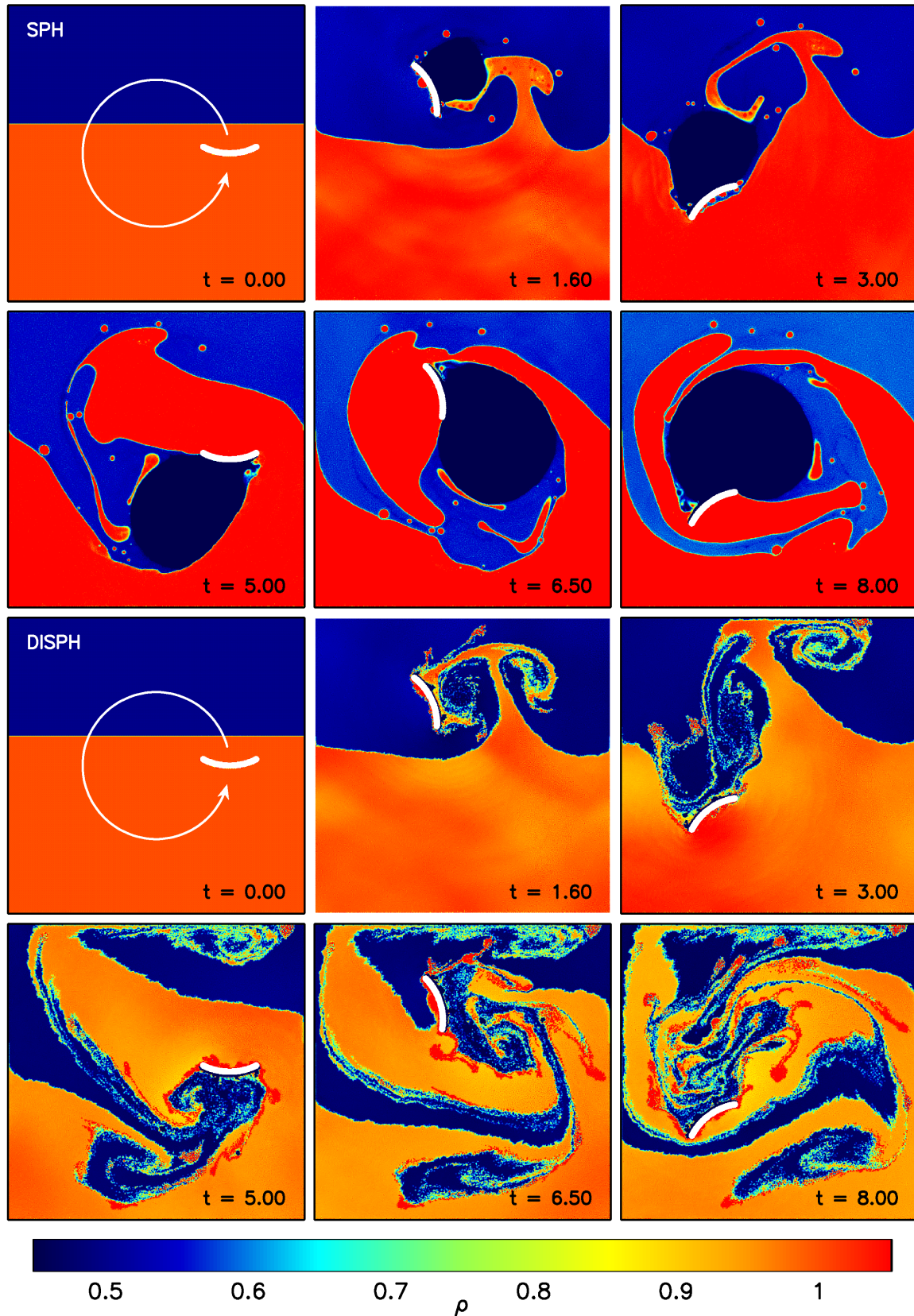
Figure 20. Evolution of the two phase fluid forcibly mixed by the spoon up to $t = 8.0$. Top six panels show the evolution using the standard SPH, while the bottom six panels show that using our SPH. The arcuate structure expressed by white points is the spoon. The white long arc (almost circle) found in the panels at $t = 0$ represents the motion of the spoon and the arrow shows the direction of the motion (the anti-clockwise). Colors predict the density of the fluid and the color bar can be found in the bottom of panels.
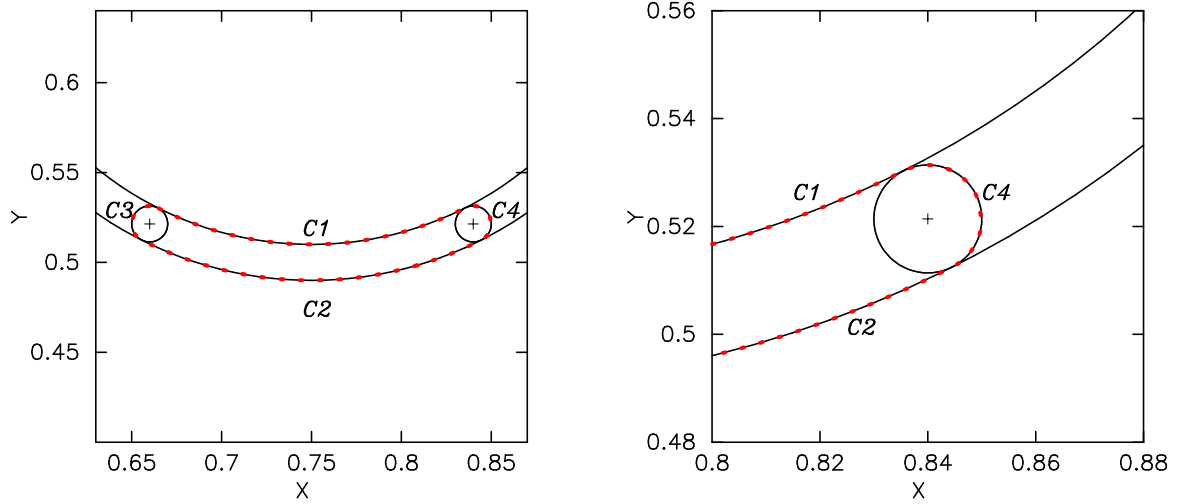
Figure 21. Shape of the spoon. Dotted curve with red color exhibits the boundary of the spoon. Circles consisting of the closed surface are also shown. *Left*: Whole region of the spoon. *Right*: Close up of the left edge of the spoon.

—. 1997, Journal of Computational Physics, 136, 298

—. 2002, MNRAS, 335, 843

—. 2005, Reports on Progress in Physics, 68, 1703

Monaghan, J. J., & Price, D. J. 2001, MNRAS, 328, 381

Morris, J. P. 1996, PASA, 13, 97

Okamoto, T., Jenkins, A., Eke, V. R., Quilis, V., & Frenk, C. S. 2003, MNRAS, 345, 429

Price, D. J. 2008, Journal of Computational Physics, 227, 10040

—. 2012, Journal of Computational Physics, 231, 759

Read, J. I., & Hayfield, T. 2012, MNRAS, 422, 3037

Read, J. I., Hayfield, T., & Agertz, O. 2010, MNRAS, 405, 1513

Ritchie, B. W., & Thomas, P. A. 2001, MNRAS, 323, 743

Rosswog, S. 2009, New Astron. Rev., 53, 78

Sedov, L. I. 1959, Similarity and Dimensional Methods in Mechanics

Sod, G. A. 1978, Journal of Computational Physics, 27, 1

Springel, V. 2005, MNRAS, 364, 1105

—. 2010a, MNRAS, 401, 791

—. 2010b, ARA&A, 48, 391

Springel, V., & Hernquist, L. 2002, MNRAS, 333, 649

Thomas, P. A., & Couchman, H. M. P. 1992, MNRAS, 257, 11

Youngs, D. L. 1984, Physica D Nonlinear Phenomena, 12, 32